8-7-2020

Microstructure design of third generation advanced high strength steels

Matthew Cagle

Microstructure design of third generation advanced high strength steels

By

Matthew Scott Cagle

Approved by:

Hongjoo Rhee (Major Professor)
Haitham El Kadiri (Co-Major Professor)
Youssef Hammi
Kamalesh Mandal
Yucheng Liu (Graduate Coordinator)
Jason M. Keith (Dean, Bagley College of Engineering)

A Dissertation
Submitted to the Faculty of
Mississippi State University
in Partial Fulfillment of the Requirements
for the Degree of Doctor of Philosophy
in Mechanical Engineering
in the Department of Mechanical Engineering

Mississippi State, Mississippi

August 2020

Name: Matthew Scott Cagle

Date of Degree: August 7, 2020

Institution: Mississippi State University

Major Field: Mechanical Engineering

Major Professors: Hongjoo Rhee and Haitham El Kadiri

Title of Study: Microstructure design of third generation advanced high strength steels

Pages in Study: 84

Candidate for Degree of Doctor of Philosophy

This dissertation demonstrates that substantial ductility improvement is possible for low-manganese transformation induced plasticity steel compositions through the quenching and partitioning heat treatment approach using a Gleeble thermo-mechanical simulator. Two investigated compositions had unique microstructures and mechanical behavior from an identical applied quenching and partitioning process. Electron backscattered diffraction analyses indicate that Comp-2 and Comp-5 both contained retained austenite which resulted in enhanced ductility. The face-centered cubic phase (austenite) more efficiently mitigates strain incompatibilities when located at martensitic grain boundaries known for hot spots and damage initiation. This location effect leads to enhanced ductility and improved toughness in a lean, transformation induced plasticity steel. However, the increase in ductility in Comp-2 and Comp-5 is limited; the partitioning of carbon cannot stabilize austenite to reach strength/ductility targets set by the Department of Energy. Comp-2 and Comp-5 lack sufficient manganese to stabilize austenite to a higher degree. Chem-2A will be explored to determine if the partitioning stage can stabilize austenite closer to the martensite finish temperature. Periodic intercritical annealing will be applied to Chem-1A to see if mechanical properties can be increased further than current

research values. Ultimately, through literature, Manganese is proven to be a more effective austenite stabilizer than carbon, and with tailored heat-treatment, the DOE targets can be reached.

ACKNOWLEDGEMENTS

I would like to first thank my Lord and Savior Jesus Christ for creating me and giving me a world to explore. I want to thank the Engineering and Research Development Center (ERDC) for funding this research and providing expertise during the project. I would like to thank my committee for their expertise and guidance during my PhD. program. I want to thank the Center for Advanced Vehicular Systems (CAVS) for expert personnel and facilities to conduct steel research. I would also like to thank the Steel Research Group at CAVS for support and guidance during my PhD. I want to thank Mississippi State University for the opportunity of graduate school. I also would like to thank the Mitchell Memorial Library and ETD Format and Submission for formatting my dissertation for library submission. I would like to thank my wife for her help editing my dissertation and support throughout my research. I also would like to thank my family for prayers, support, and encouragement during my PhD program. I want to thank all my friends at MSU and CAVS for their encouragement, support, and help during my PhD. Lastly, I want to thank my dogs, Copper and Maddie, for their constant excitement when I walked through the door.

The research described and the resulting data presented herein, unless otherwise noted, was funded under PE 0602784A, Project T53 "Military Engineering Applied Research", Task 3 under Contract No. W56HZV-17-C-0095, managed by the U.S. Army Combat Capabilities Development Command (CCDC) and the Engineer Research and Development Center

(ERDC). The work described in this document/presentation was conducted at Center for Advanced Vehicular Systems at Mississippi State University. Permission was granted by OPSEC to publish this information. Any opinions, findings and conclusions or recommendations expressed in this material are those of the author(s) and do not necessarily reflect the views of the United States Army.

TABLE OF CONTENTS

LIST OF TABLES

LIST OF FIGURES

CHAPTER I

BACKGROUND ON THIRD GENERATION ADVANCED HIGH STRENGTH STEELS

The overall goal of this PhD program was to investigate microstructure design of third generation advanced high strength steels (3GAHSS). We wanted to create novel steel compositions through advanced processing routes to secure microstructures that exceeded current mechanical properties for 3GAHSS.

During this PhD program, our three goals were the following:

1. Develop new 3GAHSS with experimental microstructures
2. Conduct microstructural characterization and mechanical testing on novel 3GAHSS
3. Evaluate mechanical properties compared to previous 3GAHSS

The previously designed steel generations are in Figure 1.1, referred to as the banana chart. Total elongation is plotted against ultimate tensile strength. The conventional steels (shown in black) have high ductility but lack strength due to primarily ferritic microstructures. The 1st generation advanced high strength steels (1GAHSS), shown in maroon, have mixed microstructures of ferrite/martensite or bainite/austenite. 1GAHSS possess higher strength compared to conventional steels, but lower ductility. Strength and ductility are mutually exclusive and improving both is a challenge. Second generation AHSS (2GAHSS) achieved this goal with heavy alloying. These steels' mostly austenitic microstructures exhibit great strength and ductility but are expensive to manufacture. 2GAHSS compositions include high alloying amounts of manganese, chromium, or nickel; which are incredibly expensive to mine. Third generation AHSS

(3GAHSS) became the research focus, with improved properties of 1GAHSS but lower manufacturing cost than 2GAHSS. Auto makers have great interest in 3GAHSS that is stronger and more ductile than previously known steel generations and cost effective.

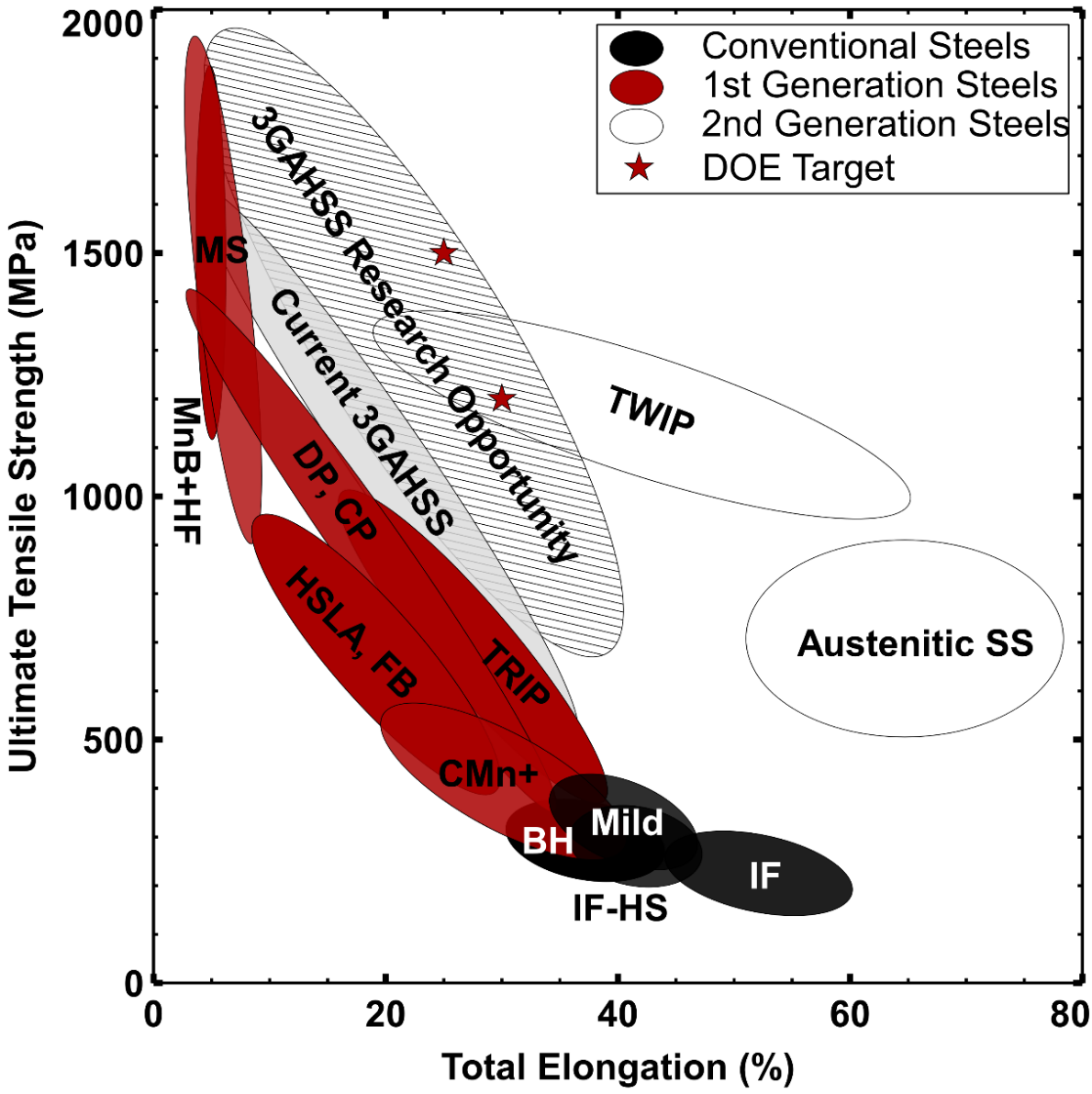

Figure 1.1 Steel generation chart showing conventional and the three generations of advanced high strength steels.

There are two benefits to this improved steel: weight reduction and safety assurance. If steel is stronger and more ductile, less steel is needed within automobile components, referred to as downgauging. Reduction of steel within an automobile leads to overall weight reduction and increased fuel economy. The second benefit of improved steel is maintaining safety with a vehicular structure. 3GAHSS offer the same or enhanced structural integrity of previous steel components. Automakers are seeking ways to reduce vehicle weight while still meeting specifications regarding crashworthiness and cost constraints. With magnesium alloys' low ductility and high strength aluminum's high manufacturing cost, 3GAHSS emerge as the most economical solution. Decreasing the required thickness/cross sections of body panels and structural members leads to mass reductions of the vehicle [1]–[5]. Among the widely adopted top-down strategies to achieve 3GAHSS, the quenching and partitioning (Q&P) method is recognized as the most affordable. Q&P uses carbon as the main γ-gene element (austenite stabilizer), in contrast to other methods using cost-prohibitive contents of either Mn or Ni [2, 5–7].

1.1 Carbon Partitioning into Austenite

Our investigation into 3GAHSS began with the quenching and partitioning (Q&P) process pioneered by Speer et al. [1]. The key element in quenching and partitioning is C partitioning from supersaturated martensite to untransformed austenite [1]. Before Speer et al. developed the quenching and partitioning process, C partitioning at high temperatures was well-known between ferrite and austenite during reconstructive transformations. These transformations where iron and other substitutional atoms diffuse in short-range movements cause a body-centered cubic (BCC) crystal to transform to a face-centered cubic (FCC) crystal. However, C partitioning after displacive transformation (coordinated atom movements) such as martensite formation is

controversial [1]. Martensite formation was believed to happen without carbon or interstitial diffusion. Conventional heat treatments such as quenching and tempering never involved temperatures where C could partition from martensite and austenite. Also, competing reactions like carbide formation would deplete the available C reservoir. Some evidence of C partitioning was observed from martensite to austenite in-between interlath films. This process occurred upon cooling or isothermal holding in steels containing silicon (Si) after the martensitic transformation. Additionally, C partitioning to austenite was possible in carbide-free bainite structures after forming through diffusionless martensite formation. The most common context for C partitioning at the time of this study was during tempering of martensite, where carbide precipitation was known to happen [1].

Speer et al. based quenching and partitioning on the idea of constrained paraequilibrium (CPE) [1]. The thermodynamics of C partitioning from martensite to austenite was not fully examined, and a model was developed to investigate this phenomenon. C partitioning from as quenched martensite to austenite could be explored with completely suppressed reactions. Cementite or transition carbide formation and austenite decomposition into bainite were precluded from this model along with C partitioning kinetics. The model assumptions allowed an endpoint of partitioning determination [1]. In equilibrium conditions, martensite and retained austenite are expected to decompose into ferrite and iron carbide. The phase compositions can be determined by lever rule from the different phase boundaries on an iron-carbon (Fe-C) phase diagram. When substitutional atoms (X) are introduced (making an Fe-C-X ternary alloy), long range diffusional processes at low temperatures are mostly C atom movements. This condition is referred to as paraequilibrium, where substitutional atoms do not partition between phases upon transformation [1]. As a result, the Fe/X ratio remains constant. Paraequilibrium condition lacks meaning without

substitutional atoms present in a steel alloy. In thermodynamic terms, paraequilibrium represents a minimum free energy condition, with additional constraint (Fe/X atom ratio does not change). Also, at paraequilibrium the phase fractions and compositions are fixed. In contrast, orthoequilibrium (Fe-C alloy) phase fractions of ferrite and austenite adjust to reach the minimum free energy condition [1]. When slow diffusing substitutional atoms are present, the free energy minimization becomes a paraequilibrium. The C potentials in ferrite and austenite are equal, but a need for metastability persists. For metastability, the interface between ferrite and austenite must migrate, adjusting the phase fractions. With the provision of a fixed interface, neither orthoequilibrium nor paraequilibrium is attainable. Speer et al. introduced a new model, constrained paraequilibrium (CPE) with the constraint being an immobile interface [1].

CPE has complete absence of Fe or substitutional atom movements, in contrast to paraequilibrium. However, C can migrate between phases as required. The C atoms only move over distances greater than a unit cell, and CPE applies to Fe-C alloys and Fe-C-X alloys. Two key provisions of CPE are as follows:

1. C diffusion is complete when the C potential in ferrite and austenite are both equal.
2. The number of Fe atoms in each phase is conserved.

The first provision represents the minimum free energy condition, while the second exhibits an immobile interface after martensite growth. CPE only requires the C potential of both phases to be equal, in contrast to orthoequilibrium, which requires both the Fe and C potentials to establish equilibrium. Figure 1.2 depicts orthoequilbrium between ferrite and austenite. The tangent line between ferrite and austenite represents the orthoequilibrium condition. Conversely, Figure 1.3 shows the constrained paraequilibrium condition where only the C potentials are equal. There are theoretical infinite set of compositions that satisfy this condition [1].

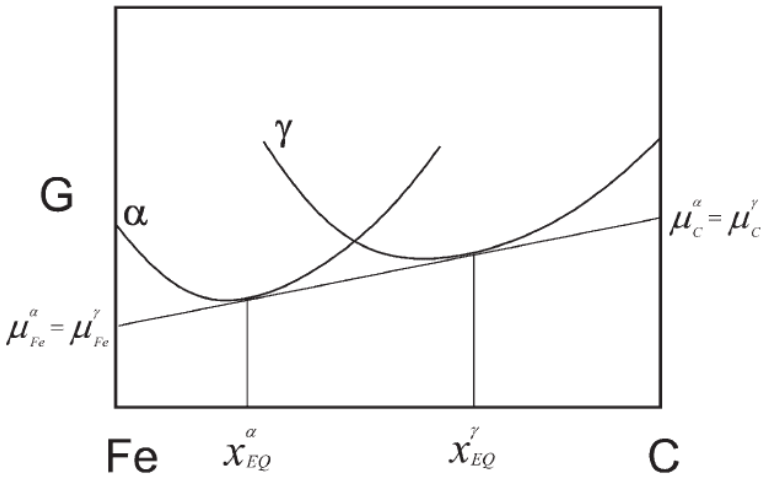

Figure 1.2 Schematic showing Gibbs free energy versus composition. The tangent line shown represents orthoequilibrium between ferrite (α) and austenite (γ). The chemical potentials for carbon and iron are μC and μFe , respectively [1]. X_{EQ} is the equilibrium composition of the given phase.

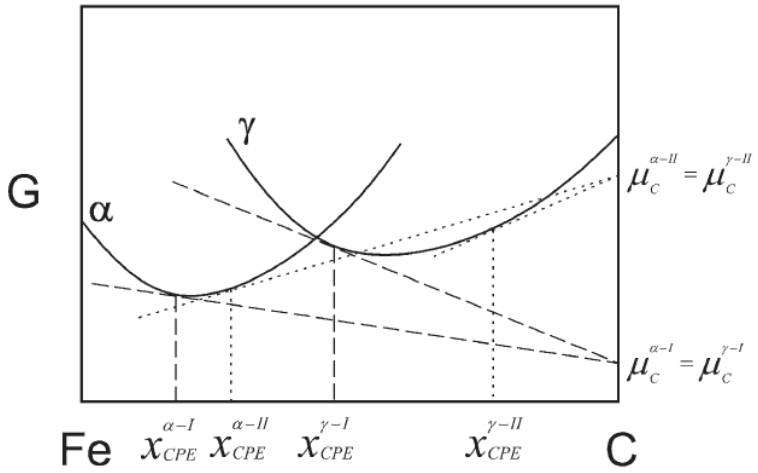

Figure 1.3 Schematic of constrained paraequilibrium (CPE) showing different compositions that satisfy the CPE condition of ferrite (α) and austenite (γ). The chemical potential for carbon is μ_C ,and X_{CPE} is the CPE composition of the given phase [1].

Speer et al. calculated different CPE conditions from 200 to 600ºC with 25, 50, 75, and 90% starting mole fractions of martensite. These temperatures were a range where substitutional

atoms do not partition. From the results, CPE was affected by composition, temperature, and initial phase fraction. Orthoequilibrium, however, is independent of composition with the phase fractions adjusting according to the lever rule. In CPE, the phase fractions only slightly change during C transfer across a constrained interface. The C concentration in ferrite increased with increasing temperature, but in austenite, the C concentration decreased with increasing temperature. This result showed greater composition dependence in ferrite than austenite and low solubility of C in ferrite. Austenite could receive the most carbon during partitioning according to the CPE condition. Phase compositions are either C enriched or C depleted relative to orthoequilibrium. When austenite fractions are greater than values at orthoequilibrium, the CPE phase compositions possess lower C levels than orthoequilibrium values. If austenite fractions are lower than orthoequilibrium, then CPE phase compositions have higher C levels than orthoequilibrium.

Cautions about Speer et al.'s work included carbon activity and composition approximations. The carbon activity used in Speer's calculations were for steel with C content well below 1%; therefore, the compositions of ferrite and austenite are approximate [1]. Some of the CPE calculations included austenite with C contents higher than 6.7 wt.%. This approximation exceeds the amount of carbon in cementite; so, imagining that carbide formation is suppressed is difficult [1]. To suppress cementite, higher levels of Si and Al are required for the quenching and partitioning process. Transformation induced plasticity (TRIP) steels are reasonable candidates which require little modification to their composition [1]. Si, Al, and P are present and help retard the formation of carbides, resulting in martensite and retained austenite at room temperature. High strength bainite free grades are useful, if allowed sufficient time to discourage carbide formation [1]. Speer contended that greater amounts of C could be partitioned to austenite with Q&P than in carbide-free bainite steels. Ferrite growth and C partitioning in carbide-free bainite steels are

effectively coupled; whereas, in Q&P steels, the initial fraction of martensite and austenite can be adjusted independent from the partitioning process. Lath or twinned martensite before partitioning could affect the final mechanical properties in Q&P steels in novel ways. As a note of explanation, constrained paraequilibrium (CPE) was renamed constrained carbon equilibrium (CCE) as a result of the discussion between Speer et al. and Hillert et al. [2–4]

1.2 Effect of Manganese on Retained Austenite

Manganese (BCC) also stabilizes austenite (FCC) at room temperature. Fully austenitic Second generation advanced high strength steels were developed using high alloying amounts (up to 30 wt.%) of Mn [11]. These steels boast higher ductility than first generation advanced high strength steels mostly due to twinning induced plasticity (TWIP). The austenite in TWIP steels is very stable at room temperature, and during straining, deformation twins form in austenite grains. The austenite resists the TRIP effect and continues to remain FCC at higher strain levels. Miller et al. examined a medium manganese steel composition in 1972 and found that ultra-fine grain structures can mechanically stabilize austenite [12]. Cold rolling followed by intercritical annealing led to enhanced austenite stability. Navara et al. also investigated manganese effect in steels, reporting that austenite growth rate changes from C diffusion control to Mn diffusion control at critical temperature, A_{C1} [13]. Closer to the A_{C1} or lower bound of intercritical annealing, Mn diffuses more effectively into austenite. This feature is due to a free energy decrease in austenite as a function of Mn content inversely related to temperature. Also, Mn in cementite lowered the C activity supplied to austenite. Different austenite growth rates were expected with gradients of Mn diffusion [13]. Speich et al. found austenite formation begins at dissolved pearlite, then grew into ferrite before slow homogenization of austenite islands through Mn diffusion [14]. At a sufficiently low intercritical temperature (750 C for this study), Mn diffusion in ferrite or

along ferrite grain boundaries controlled austenite growth rate. Navarra et al.'s experiments revealed a segregation of Mn during cooling [13]. The growth of austenite was associated with ferrite boundary migration. The phase boundaries were enriched with Mn, unless the region was very small. Diffusion induced grain boundary migration (DIGM) was discussed here, where austenite forms behind a migrating ferrite boundary. DIGM effect was confined to a certain temperature range where grain boundary (GB) diffusion was significantly higher than lattice diffusion. This diffusion effect is typical for substitutional alloy systems because of concentration gradients [13]. The boundary migration could occur anywhere on a boundary, sometimes in the opposite direction of the boundary. The zone behind the migrating boundary became enriched in Mn, which helped encourage austenite formation. Figure 1.4 illustrates the formation of austenite along ferrite grain boundaries (GB) [13]. First, the ferrite GB migrated leaving behind Mn enriched areas for austenite nucleation. Next, the austenite formed, followed by austenite growing through Mn diffusion controlled through the ferrite lattice. However, the diffusion of Mn into austenite is very sluggish, explaining the reason for Mn concentrations at the GBs. Sun et al. found that Mn partitioning occurred in dual phase (DP) steels through 3 stages (similar to Speich et al. [14]) [15]. Stage 1 is austenite formation through pearlite dissolution which was rapid and controlled by C diffusion. In Stage 2, the nucleated austenite grows in ferrite grains and ferrite grain boundaries, which is controlled by C and Mn diffusion. Finally, in Stage 3, austenite moved towards equilibrium where the concentration gradients of C and Mn were eliminated [15]. Sun and Pugh modeled Mn partitioning between ferrite and austenite using needle-like austenite contained in ferrite [15]. Both phases were considered as cylinders to simplify the model, and Mn diffusion was only considered in the radial direction.

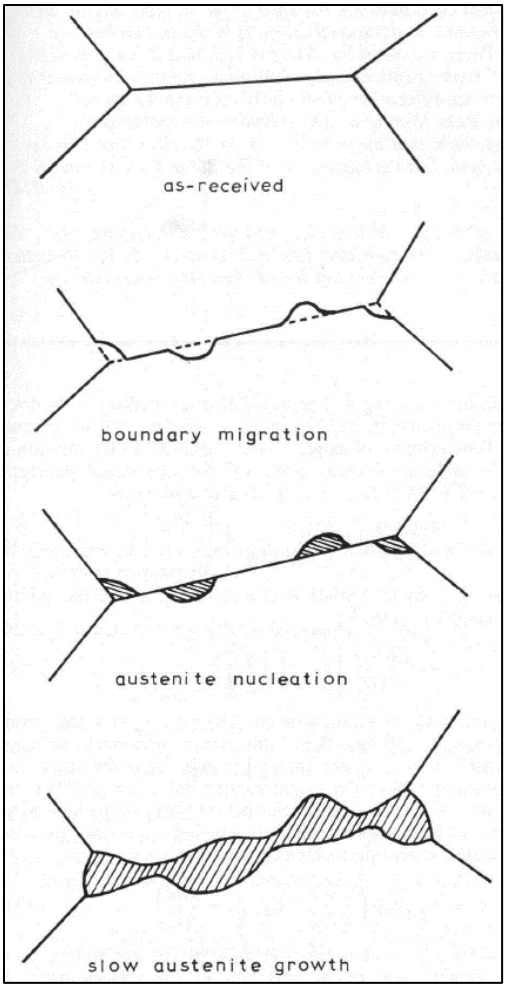

Figure 1.4 Schematic of austenite nucleation and growth along ferrite grain boundaries because of diffusion induced grain boundary migration (DIGM) [13].

A higher than soluble Mn concentration was present in ferrite and lower than solubility Mn concentration was present in austenite. As a result, the Mn diffuses from the ferrite to austenite and creates a Mn-rich rim between the ferrite and austenite. This created rim results from ferrite's three orders of magnitude higher Mn diffusion rate. Mn diffusion continues until no Mn gradient exists between ferrite and austenite. Lis et al. also explored Mn partitioning [16]. Annealing at 625ºC with holding times from 1 hour to 60 hours, they found evidence of Mn partitioning longer

than annealing for 3 hours. Stable austenite was present after 10 hours, and Mn concentration in austenite and carbides increased with longer annealing times.

De Moor et al. proposed a model to predict austenite stabilization through Mn partitioning [17]. This model, like the Speer et al. model, predicted retained austenite at room temperature. Instead of choosing quench temperature, annealing temperature is chosen. The Koistenin-Marburger equation was used as seen in Equation 1.1 [18],

$$f_M = 1 - e^{-0.011(M_S - T)} \tag{1.1}$$

Where f_M is the amount of fresh martensite that formed upon cooling, M_s is the martensite start temperature, and T is the temperature quenched to (25ºC). De Moor et al. subtracted the amount of fresh martensite from the austenite formed during intercritical annealing, to calculate the amount of retained austenite at room temperature [17]. Figure 1.5 shows this model with different annealing temperatures selected.

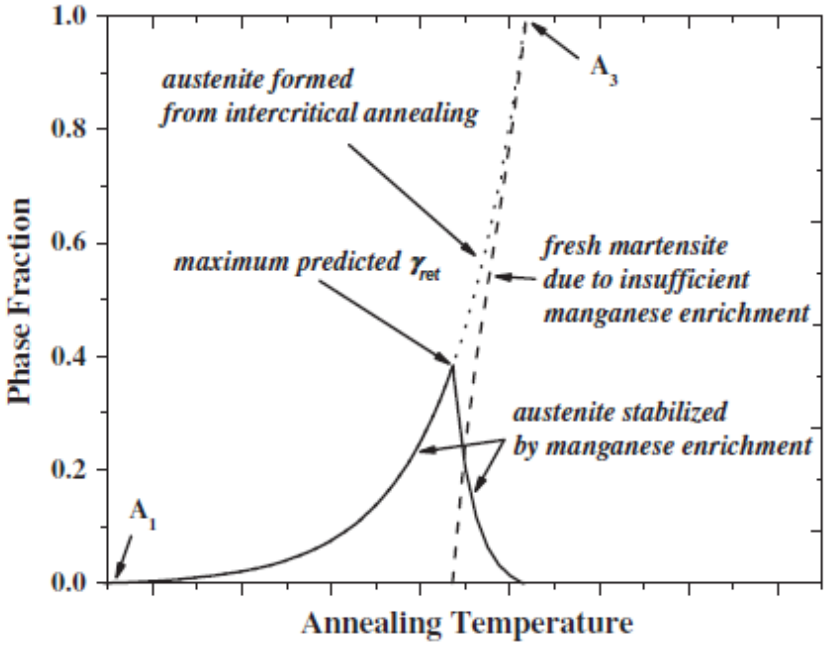

Figure 1.5 Predictive model of retained austenite after intercritical annealing. This model uses Mn enrichment to stabilize austenite upon subsequent cooling to room temperature [17].

A maximum amount of retained austenite (0.4 volume fraction) was obtained at a given annealing temperature. Similarly, Lee et al.'s experiments showed austenite was very stable when enriched with Mn [19]. Dilatometric samples were annealed at from 640 to 700ºC for 180 s. In the 640, 660, and 680ºC samples, austenite did not transform to martensite upon cooling, which meant the respective martensite start (M_s) temperatures were below -150ºC [19]. The austenite islands in the 640ºC sample received the highest Mn enrichment.

Gibbs et al. performed one week intercritical annealing (IA) at temperatures from 575 to 675ºC for a medium manganese steel [20]. Figure 1.6 shows the austenite stability curves for the intercritically annealed samples. The resulting austenite stability was highest for the 575ºC sample and lowest for the 675ºC; however, the sample with the optimal austenite stability was the 600ºC sample [20]. Roughly 2/3 of the austenite transformed after 10% strain, leading to the maximum

ductility reported. The austenite was stabilized enough to resist TRIP for a certain strain range, but not stable enough to resist transformation completely. The amounts of Mn within each IA sample were 15 to 8%, respectively, and the ultra-fine grain structure allowed the Mn to diffuse quicker and stabilize the austenite. De Cooman et al. also explored IA at 600ºC and 650ºC for one week [21]. The 650ºC experienced rapid austenite transformation to martensite, mostly stress-assisted, but the 600ºC sample showed a constant transformation rate due the austenite stabilized by Mn. Ultimately, the yielding of these two IA steels was controlled by the stability of the austenite islands. De Cooman et al. introduced the idea of a M_S^{σ} temperature that separated the stress-assisted and strain-induced regions of austenite transformation [21]. In the stress-assisted region, martensite nucleates on existing sites enhanced by stress. Conversely, in the strain-induced region, martensite forms on nucleation sites made by slip bands.

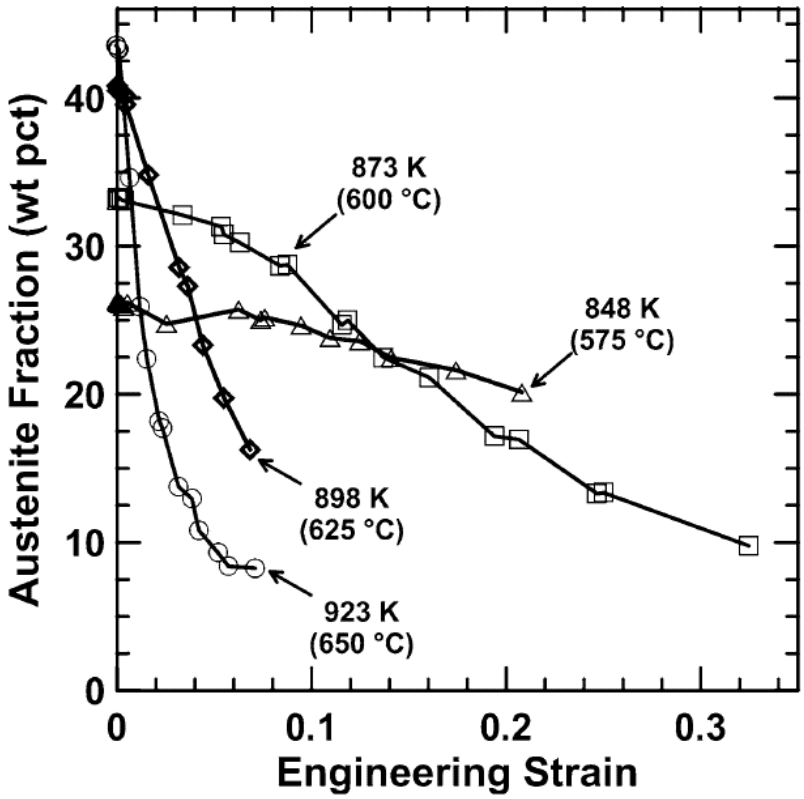

Figure 1.6 Austenite stability plotted against engineering strain. 575ºC has the flattest curve (highest austenite stability) and 650ºC has the steepest curve (lowest austenite stability). 600ºC shows an optimum austenite stability with the highest achieved ductility.

Gibbs et al. performed interrupted tension tests with neutron diffraction to observe austenite transformation through strain progression [22]. Two different IA temperatures to enrich austenite with Mn were examined: 600ºC and 650ºC. The 650ºC sample experienced stress-assisted austenite transformation to martensite, and the 600ºC sample showed strain-induced austenite transformation to martensite. The 650ºC sample exhibited lower austenite stability than the 600ºC sample which caused extensive plastic deformation in austenite via slip. The austenite in the 650ºC transformed very quickly, resulting in dual phase behavior after austenite

transformation ceased. Some austenite remained in the 600ºC after failure, highlighting the superior stability present in the steel. Han et al. discovered austenite transformation ratio (ATR) increased with longer annealing times. The ATR is calculated by Equation 1.2,

$$ATR = \frac{(V_{\gamma-UD} - V_{\gamma AF})}{V_{\gamma-UD}} * 100 \quad (1.2)$$

where $V_{\gamma-UD}$ is the volume fraction of undeformed austenite, and $V_{\gamma AF}$ is the volume fraction of austenite after failure. The medium manganese steel in Han et al.'s study was annealed from 3 minutes to 12 hours at 640ºC. Mn diffusion into austenite was very slow, resulting in sluggish recovery and recrystallization of austenite. Cai et al. determined that high austenite stability is required for the maximum TRIP effect [23]. Austenite can possess different stabilities within an intercritically anneal medium manganese steel, causing a discontinuous TRIP effect [23]. Each austenite stability was dependent on composition – the higher the Mn and C concentration, the higher the austenite stability. Small grain size also stabilizes austenite by preventing TRIP through mechanical restraint of neighboring ferrite grains [23]. Cai et al. performed intercritical annealing at 750ºC for 3-10 minutes followed by water quenching. Energy dispersive spectroscopy (EDS) showed Mn partitioning from delta ferrite into austenite in all the samples. In the 3-min annealed sample, more Mn was found in intercritical ferrite than austenite, which had non-uniform distribution of Mn, whereas the 10-min annealed sample contained uniform Mn content in austenite. The 3-min sample had superior mechanical properties compared to the other samples because of different austenite stabilities. These different austenite stabilities contributed to a discontinuous TRIP effect, meanwhile the other samples had a weakened TRIP effect. The 7-min

and 10-min samples contained higher and uniform austenite stabilities, but the larger grain size decreased the steel's strength.

1.3 Quenching and Partitioning Process

Q&P of steel begins with full austenitization above A_{C3} critical temperature or intercritical annealing between A_{C1} and A_{C3}. Next, the steel is rapidly quenched to a temperature between martensitic start (M_S) and martensitic finish (M_F). Finally, the steel is held at the quench temperature (1-step Q&P) or reheated to a partitioning temperature (2-step Q&P) before quenching to room temperature [1, 14–16]. The microstructural evolution that occurs during this process starts with 100% austenite or a set fraction of austenite and intercritical ferrite. After the first quench, an initial fraction of athermal martensite and austenite is set. During partitioning (either at 1-step or 2-step), the athermal martensite is supersaturated in carbon, which diffuses and chemically stabilizes austenite. Upon final quench, the microstructure yields C depleted martensite and C enriched austenite. Rapid quenching promotes nucleation of martensite and avoid formation of intermediate phases which would impair strength [26]. With stabilized austenite, attractive mechanical properties were achieved and reported by many authors [2, 5, 23]. Q&P steels experience a well-known phenomenon known as the transformation induced plasticity (TRIP) effect. Under deformation, austenite transforms to martensite, delaying the onset of necking and enhancing the ductility of the steel.

Two major design constraints exist with quenching and partitioning: quench temperature and partitioning temperature/time. The first constraint is quench temperature selection, which is critical to setting an appropriate volume fraction of martensite and austenite. The quench temperature is unique to the steel composition chosen for Q&P. Quenching too high results in a large volume fraction of austenite, but insufficient carbon is available in the supersaturated

martensite to stabilize the austenite [28], [29]. Fresh martensite forms upon quenching to room temperature; as a result, a lower volume fraction of retained austenite is obtained. Quenching too low results in a large fraction of austenite that is consumed due to proximity of the martensite finish temperature. A surplus carbon supply is available to stabilize the small volume fraction of austenite [29]. The optimum quench temperature can be found through three assumptions related to constrained carbon equilibrium:

1. All the carbon partitions to austenite.
2. The kinetics of partitioning are precluded.
3. Competing reactions during partitioning are completely suppressed.

The Koistinen-Marburger relationship was used to calculate the volume fraction of martensite that formed during initial quench and final quench by undercooling. The optimum quench temperature is then found, yielding the maximum volume fraction of retained austenite. Figure 1.7 shows a calculated optimum quench temperature for a 0.19%C-1.59%Mn-1.63%Si steel [29]. The peak, located at roughly 240ºC, gives the maximum volume fraction of retained austenite for this steel. As Figure 1.7 shows, there is quench temperature sensitivity present in this steel, shown by Clarke et al. [29]. The chosen quench temperature will determine the initial fraction of athermal martensite and untransformed austenite as seen in Santofimia et al.'s study [30]. They applied quenching and partitioning to 0.19C-1.61Mn-0.35Si-1.10Al-0.09P(wt.%) TRIP steel. Quenching occurred at 125, 150, or 175ºC for 3 s, and partitioning happened at 250 or 350ºC for 3, 10, 100, or 1000 s [30]. The conclusion from Santofimia et al. was different quench temperatures do not result in significant microstructural differences.

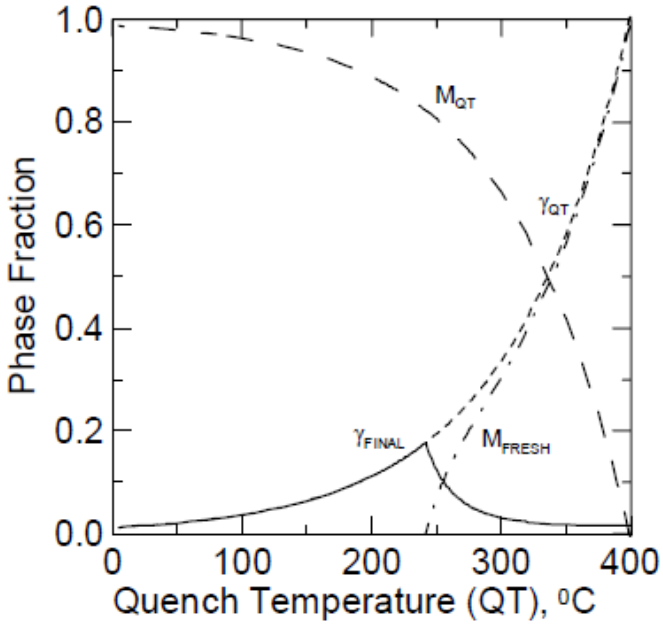

Figure 1.7 Phase fraction versus quench temperature for a 0.19%C-1.59%Mn-1.63%Si steel. The optimum quench temperature is around 240ºC given by the peak of the solid curve. Retained austenite at room temperature is γFinal. MFresh is fresh martensite that forms upon final quench. The volume fraction of austenite at quench temperature is γQT , and MQT is the martensite volume fraction after initial quench [5-6].

This discovery led future researchers to select one quench temperature sufficient for their given steel composition [31]–[33]. Using quench temperatures of 180, 295, and 320ºC, Clarke et al.'s study included carbon partitioning kinetics using DICTRA calculations for full austenization with a partitioning temperature of 400ºC [29]. Different partitioning times (Pt) from 0.0001 to 10 s were used, and for the 0.1 s Pt, the maximum volume fraction of austenite was achieved independent of quench temperature. Partitioning for longer times (up to 10 s) resulted in the same amount of retained austenite at room temperature. The results meant the sensitivity of quench temperature selection may not be as strong as originally thought, supporting Santofimia et al's claim [30]. Therefore, the processing window of Q&P steels could be expanded for large scale production [29].

The second design constraint is partitioning temperature/time. Partitioning must be long and hot enough to diffuse sufficient carbon from martensite to austenite but not too long or hot to prevent losing carbon in favor to carbide formation [27]. Clarke et al. examined partitioning times (Pt) from 0.00001 s to 10 s at 400ºC partitioning temperature (PT) [32]. They found that 0.1 s was the optimal partitioning time with the maximum retained austenite (RA) volume fraction (VF). This study included partitioning kinetics that were excluded from previous Q&P research [29]. De Moor et al. chose different partitioning times and temperatures for a 0.17C-1.65Mn-0.38Si-1.11Al-0.08P steel [24]. The result was a maximum RA volume fraction of 15% and 13% for the 400ºC and 450ºC, respectively. Increased PT may decrease internal stresses, which can influence the transformation behavior [24]. Santofimia et al. performed Q&P experiments with 250ºC and 350ºC PT and 3, 10, 100, and 1000 s Pt [30]. No carbide precipitation was seen for Pt of 3 s, but longer Pts resulted in carbide precipitation. At the 250ºC PT, substantial differences were not seen in the microstructure. Tempering of martensite did not occur for Pt less than 100 s at 250ºC PT, and carbide precipitation only happened at 1000 s Pt. For PT of 350ºC and Pt of 10 s, epitaxial ferrite and intercritical ferrite were observed [30]. Pts of 3 s and 10 s were not long enough for carbon to stabilize austenite. After Pt of 1000 s, bainite was present in all partitioned microstructures, indicating some austenite decomposed, and some austenite became enriched with C because of the formed bainite [30].

Zhong et al. also studied different Pts of 10, 20, 40, 180 s at 400ºC PT [31]. Their Q&P process was applied to a Fe–0.2C–1.5Mn–1.5Si–0.05Nb–0.13Mo(wt.%) steel. PT was chosen to produce fine carbides with the Nb additions, leading to precipitation strengthening. The resulting VF of austenite for the Pts were 4.5%, 7.0%, 5.4%, 5.2% and 5.8%, respectively. This result means 20 s was the optimal partitioning time for maximum retained austenite. The Nb and Mo additions

possibly consumed C during partitioning, and Zhong et al. suggested a steel without these elements may require a shorter partitioning time. Additionally, interface migration between austenite and ferrite during partitioning is examined within the study. The direction the interface moves could be dependent on C potential in a Q&P steel [31]. The interface is free to move from austenite to martensite or vice versa; in Zhong et al.'s work, the interface moved towards austenite, meaning less austenite was available with increasing partitioning time. Clarke et al. addressed partitioning kinetics for Pts from 0.00001 to 10 s at 400ºC [32]. The result was 0.1 s of partitioning was enough for the maximum VF of austenite, with longer times presenting the same VFs [32]. An isothermal transformation of martensite was observed by Kim et al. [34]. During partitioning, an expansion during dilatometry studies was measured that was not fully bainitic or martensitic. This expansion was the first time an isothermal transformation was identified in the Q&P process [34]. During this transformation, C atoms partition from the athermal martensite to the untransformed austenite or carbides. Conversely, the usual athermal martensite formed by rapidly quenching to room temperature. C diffusion can only take place if the cooling rates are slower, or in the Q&P case, interrupted by partitioning [34].

Santofimia et al. investigated interface migration of PTs 350ºC and 400ºC with three different values for activation energy: infinite, 180kJ/mol, and 140kJ/mol[30]. Infinite corresponded to an immobile interface, while 180 kJ/mol was a semi-coherent interface. An incoherent interface with 140 kJ/mol activation energy was based on experiments by Krielaart and Van der Zwaag with martensite and austenite film morphology [35]. Santofimia et al. showed that for the immobile (infinite activation energy) and incoherent (140 kJ/mol) interfaces, the partitioning time required for full C equilibrium was significantly lower than the semi-coherent (180 kJ/mol) interface [4]. This observation was true for the 350ºC and 400ºC PT, but at different

timescales (10 s and 1 s, respectively). Therefore, the interface mobility had a profound effect on the C kinetics during partitioning [4]. The interface for the 180 kJ/mol case was immobile until 10 s for 350ºC PT and 1 s for 400ºC PT. After that, the interface moved from martensite to austenite with progressive C enrichment until full equilibrium was reached. In the 140 kJ/mol case, C partitioning was compensated by interface migration (IM) from austenite to martensite. the interface reversed direction when the C content of austenite was lower than equilibrium, and IM ended when full C equilibrium was reached [4]. De Moor et al.'s experiments examined a PTs of 400ºC and 450ºC for 10, 30, 100 s and 10 s Pt, respectively. There was a peak of austenite (roughly 9%, 15.4%, and 14%) for the 3 TRIP steel grades after partitioning at 400ºC for 30 s. Most of the 0.2C–3Mn–1.6Si and 0.3C–3Mn–1.6Si grade samples showed exceptional ductility and strength, but the 0.3C–5Mn–1.6Si grade possessed low ductility. C diffusion during partitioning did not take place due to presence of fresh martensite after final quench; therefore, the 0.3C–5Mn–1.6Si grade may not have received an optimized Q&P process [5]. Santofimia et al. also examined different partitioning temperatures and times on a 0.2C–2.5Mn–1.5Ni–1.0Cr–1.5Si steel. PT of 350ºC, 400ºC, and 450ºC with Pts of 3 s, 10 s, 100 s, 500 s, 1000 s, and 2000 s were all applied on dilatometric samples. Isothermal transformation was observed, presumably growth of martensite [36]. The largest VF of austenite was observed in the 350ºC samples which increased to 0.15 at 2000 s Pt. Austenite VF increased with partitioning time. The average C content in austenite was between 0.75 wt.% and 0.95wt.%. Partitioning at 400ºC yield a maximum austenite VF of 0.10 after 100 s Pt. Longer Pt resulted in the same amount of retained austenite. At 450ºC, a maximum of 0.12 was seen at Pt of 3 s. A gradual decrease in austenite VF occurred up to 500 s Pt, then remained constant. This study showed that higher PT resulted in lower Pt for maximum retained austenite, which agreed well with carbon partitioning kinetics [4].

1.4 Intercritical Annealing

We also investigated intercritical annealing (IA) between critical temperatures A_{C1} and A_{C3} of medium manganese (5 to 12 wt.%) steels. IA stabilizes austenite through Mn partitioning from ferrite. Miller et al. investigated a 0.11C – 5.7Mn cold-rolled steel when held at temperatures between 520ºC and 720ºC [12]. They found that austenite began forming at 500ºC rather than 650ºC as indicated by the inflection in the hardness curve. The ultra-fine grained austenite from cold-rolling with Mn enrichment from IA led to highly stable austenite [12]. Any austenite formed above 650ºC transformed to martensite upon cooling to room temperature. Cold-rolling before IA increases rate of austenite formation, depending on the severity of cold working [12]. Thus, more austenite forms with greater reduction during cold rolling. Figure 1.8 shows this cold working effect on a medium manganese steel from Miller et al.'s work [12]. In Figure 1.8 (a), the original martensite is present after 16 hours of annealing at 600ºC. However, in Figure 1.8 (b), cold working before annealing for 16 hours at 600ºC yields an equiaxed ferrite/austenite microstructure.

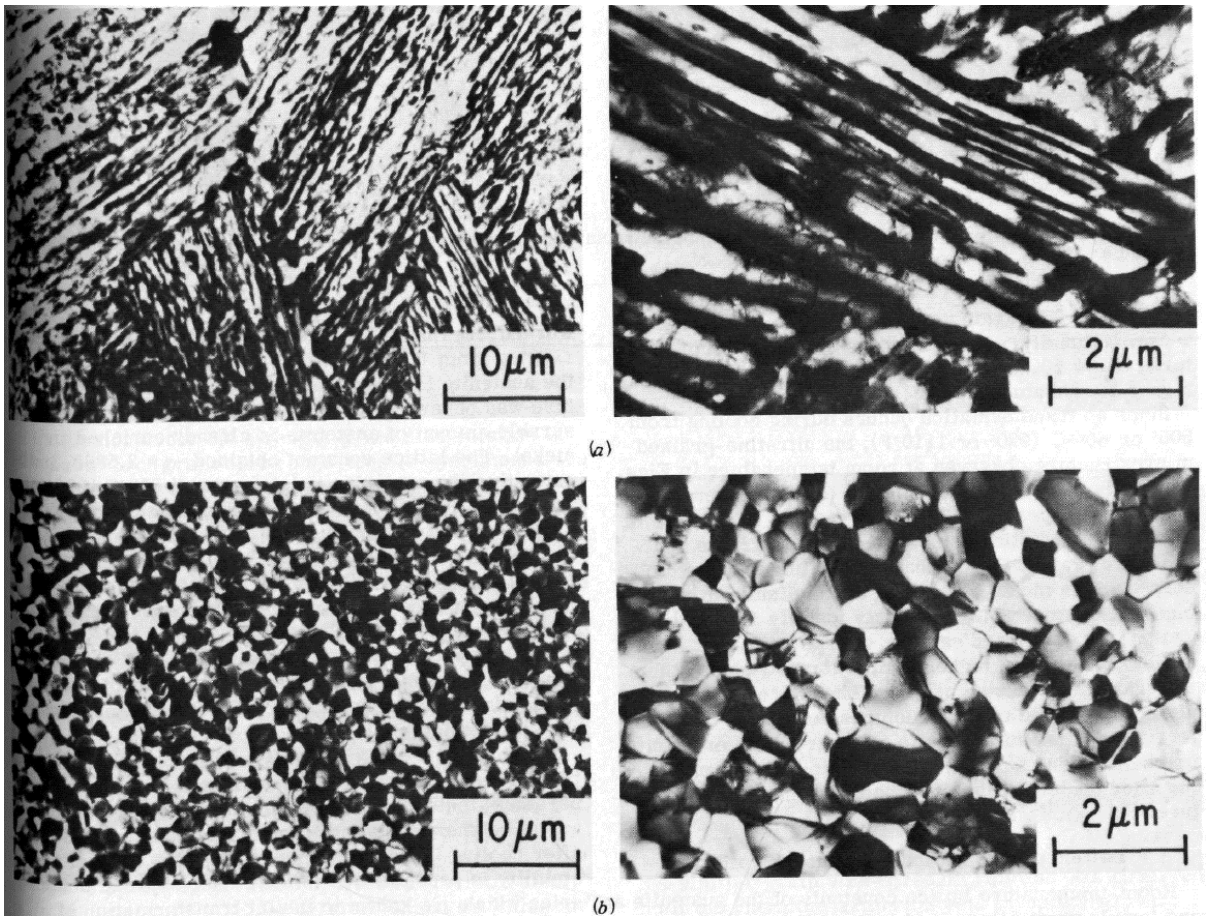

Figure 1.8 Micrographs of a) medium manganese steel annealed for 16 hours at 600ºC; b) cold worked and annealed for 16 hours at 600ºC [12].

Navarra et al. performed similar intercritical annealing at 700ºC and 725ºC from 10 minutes to 12 hours on a hot-rolled 0.1C – 1.5 Mn – 0.25 to 0.5Si commercial steel from SSAB steel company [13]. After IA at 725ºC for 10 minutes, martensite surrounds the ferrite grain boundaries; pearlite is absent that was seen in the as received steel. Austenite growth occurred independent of pearlite location, and pearlite dissolved rapidly and provided C to the austenite. There was a waviness seen between the ferrite/austenite interface. Ferrite boundary migration occurred with austenite forming behind the boundary, which contrasted austenite formation during step cooling along ferrite grain boundaries [13]. At 725ºC for 60 minutes showed austenite and

martensite growth with more equiaxed shape than 10-min sample. The austenite filled out and created impingement of grains. The sample IA at 700ºC for 60 minutes gives a better picture of austenite growth through boundary migration. Transmission electron microscopy (TEM) revealed martensitic/retained austenitic (RA) regions bulging out from two sides of a ferrite boundary [13]. A high concentration of Mn was found in the martensite/RA region with neighboring areas of Mn deficient ferrite. The boundaries between ferrite and martensite/RA were distorted, suggesting boundary migration during IA. The phase boundaries were Mn enriched unless they were very small; the leading edge of the boundary of the growing region contained more Mn than the trailing edge. However, X-ray diffraction beam overestimated the Mn content, and atom probe measurements would give better Mn estimates [13].

Huang et al. performed IA on a 0.12C– 5.10Mn–0.0040P-0.009Si–0.064Al–0.0018N steel at 650, 675, and 700ºC for 20 minutes, 1 hourr, 3 hours, 6 hours, and 26 hours [37]. Samples were water quenched following IA. RA was insensitive of the cooling rate (furnace cooling versus water quenching). The maximum volume fraction of RA was 30% for the sample annealed at 650ºC for 3 hours. The amount of martensite formed upon water quenching was higher for IA times greater than 3 hours (Figure 1.9). The amount of initial austenite was plotted against the RA amount after water quenching. The greater the gap between points A and B, the larger volume fraction of martensite formed upon water quenching [37]. The 26-hr sample contained the lowest volume fraction (%) of RA, around 1%. Conversely, the smaller the gap between A and B, the greater stability of austenite. Up to 3 s, the stability of austenite was high (at 0.6 for the V_{f_R}/V_f ratio). After 20 minutes at 650ºC, the austenite formed at prior austenite grain boundaries and fine lath boundaries. Small austenite particles (1 micron or less) were seen in the 20-min and 3-hr samples

that nucleated from fine carbides in original bainite structure. Longer annealing times resulted in growth/coalescence of these particles and martensite formation.

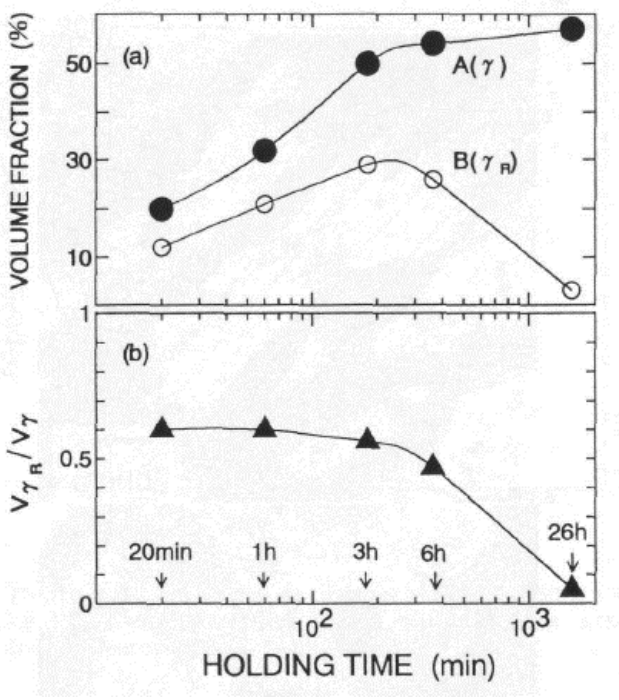

Figure 1.9 Amount of retained austenite (RA) versus intercritical annealing (IA) holding time at 650ºC. Vf is initial volume fraction of austenite formed during IA, and V_(f_R) is the RA amount after water quenching [37].

Merwin et al. investigated IA of a medium manganese steel with residual alloying amounts to simulate commercial product [38]. IA was performed from 538ºC to 732ºC either in cold spot (IA temp reached then sample cooled) or hot spot (IA temp reached and maintained for 24 hours before cooling) configuration. Microstructure etched with LePera's reagent showed evidence of banding between the original martensite and newly formed martensite/RA. The highest volume fraction of RA was 18% for Alloy 64 annealed at 650ºC. Although no measurements of RA were taken above 650ºC, the austenite carbon content was thought to dilute at higher temperatures,

making the RA amount lower. Lis et al. observed a 6Mn16 steel subjected to IA at 625ºC (below Ac_1 temperature) and 650ºC (in-between Ac_1 and Ac_3) [16]. The holding times were 1 hour, 3 hours, 10 hours, and 60 hours. Carbide spheroidizing was seen with transmission electron microscopy (TEM) after 3 hours of IA (very visible at 60 hours) [16]. The longer IA times had small influence on the coarsening of carbides, and temperature had a greater effect [16]. The phase transformation on carbide/ferrite interfaces was enhanced by C diffusion in the grain boundary and Mn diffusion in austenite layers. Longer annealing times resulted in grainy, stable austenite due to high Mn content.

Kim et al. examined 3 different medium manganese steels that were intercritically annealed from 610ºC to 800ºC [33]. The hold times ranged from 2 minutes to 24 hours. Alloy-1 showed an initial microstructure of α' martensite. After IA at 650ºC for 24 hours, Alloy-1 had an equiaxed microstructure of ferrite and austenite (Figure 1.10) with grain sizes of 0.6μm and 0.8μm, respectively [33]. The volume fraction of austenite, found by electron backscatter diffraction (EBSD), is 37% for Alloy-1 after IA. Alloy-2 showed α' martensite and ferrite initially, but after IA at 780ºC for 2 minutes, the deformed ferrite recrystallized and new ferrite/austenite formed in the deformed α' martensite (Figure 1.11) [33]. Large, elongated grains corresponded to existing ferrite, while the small equiaxed grains were new ferrite grains formed from martensite reversion.

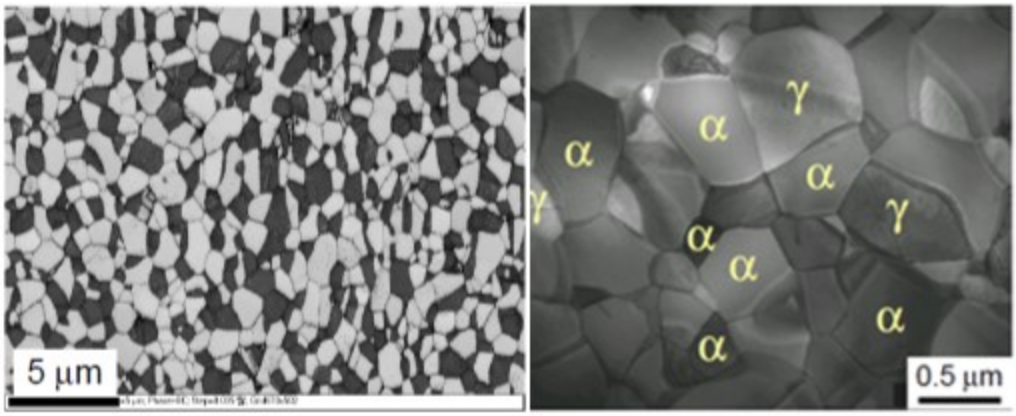

Figure 1.10 Alloy-1 intercritically annealed for 650ºC for 24 hours in a) EBSD map of ferrite (light gray) and austenite (dark) and b) STEM image showing the same microstructure [33].

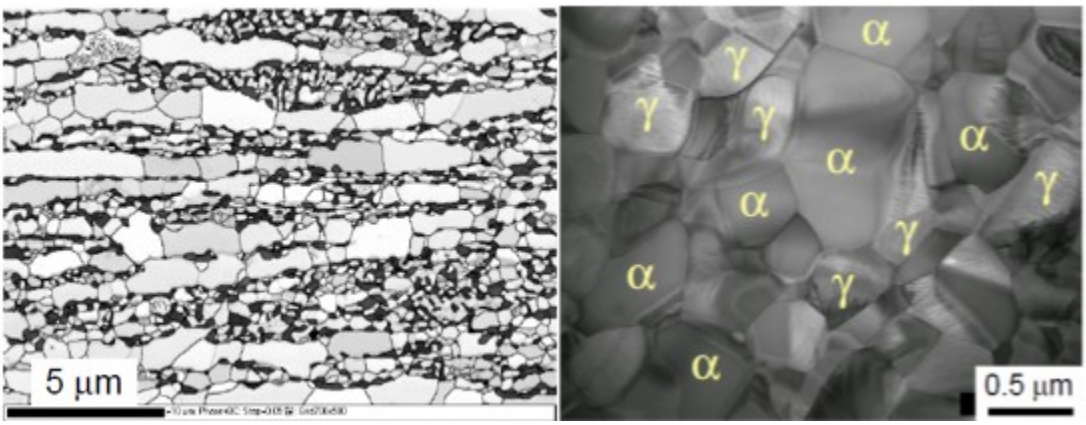

Figure 1.11 Alloy-2 intercritically annealed for 780ºC for 2 minutes in a) EBSD map of ferrite (light gray) and austenite (dark) and b) STEM image showing the same microstructure [33].

Alloy-2 had a RA volume fraction of 29% measured with EBSD [33]. In the samples IA at 760ºC and 800ºC, the RA volume fractions were 20% and 10%, respectively. Alloy-3's microstructure was initially α' martensite and negligible amounts of ε martensite. After IA for

620ºC, there was a 95% volume fraction of austenite present [33]. Figure 1.12 depicts the EBSD image of Alloy-3 after IA. Fine austenite grains that form during martensite reversion help stabilize austenite upon cooling to room temperature [33]. In the 600ºC and 640ºC samples, both had austenite volume fractions above 90%. De Moor et al. proposed a model to predict the amount of RA from Mn partitioning during intercritical annealing [17]. Full Mn partitioning was assumed along with suppression of diffusion transformation products. The RA amounts were predicted based on the IA composition of austenite. The amount of fresh martensite found by the Koistenin-Marburger relationship was subtracted from the austenite fraction formed during IA. De Moor et al.'s model was applied to Miller et al.'s experiments [12] using Thermo-Calc for initial phase fractions and equilibrium C and Mn concentrations in austenite [17]. A pronounced peak was seen in the C content as a function of IA temperature, which correlated to cementite dissolution. The Mn content in austenite decreased with increasing IA temperature as austenite fractions dilute the microstructure [17]. The M_s temperature was calculated for each IA temp to predict amounts of fresh martensite upon quenching to room temperature. A similar trend was observed comparing Miller et al.'s experiments and De Moor et al.'s model predictions[12, 17]. The predicted peak temperature is 50ºC lower than the experimental value, and the predicted RA fraction is 7% lower than experimental value [17]. Diffusion kinetics were not included in this model, and the thermodynamic table accuracy could cause errors in predicted values. Also, Mn gradients most likely existed with IA medium manganese steel. De Moor et al. concluded the cold-rolled microstructures were better suited for austenite stabilization that hot-rolled due to short diffusional distance [11, 33].

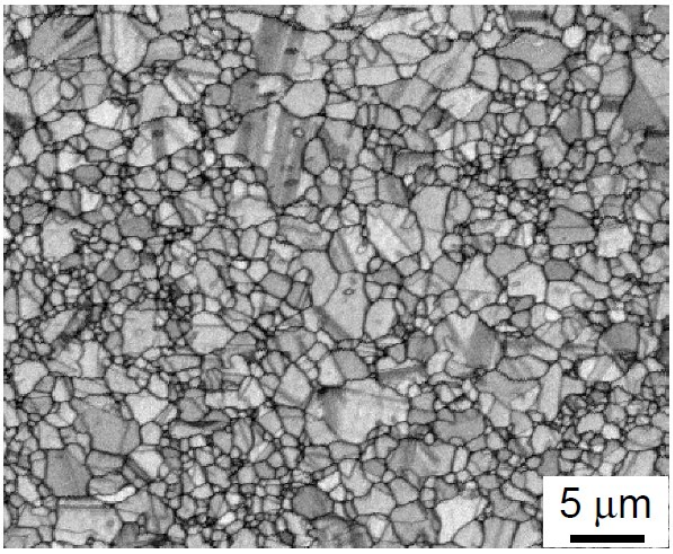

Figure 1.12 EBSD image of Alloy-3 after IA at 620ºC. The average grain diameter is 3µm.

Gibbs et al. performed IA at 575 to 675ºC for 168 hours on a 0.1C-7Mn-0.13Si steel [20]. In situ neutron diffraction was performed on the samples at different strain increments. This testing elucidated phase development under deformation. The RA volume fraction was found by Rietveld analysis [39]. The 650ºC sample contained the highest initial RA (43.5 wt.%), and 675ºC had the lowest (1 wt.%). The 675ºC IA sample likely exhibited the highest RA amount during IA, but most of this austenite was unstable and transformed to martensite upon quenching to room temperature. The experimental values of RA plotted against IA temperature matched the shape of De Moor et al.'s model [14, 16] with slight shift towards peak at higher IA temperature. Mn enrichment may have affected kinetics during IA. The 575ºC sample was 76 wt.% ferrite and 26 wt.% austenite. RA present in this sample was separate interlath islands with martensite. The 600ºC sample was 49 wt.% ferrite, 18 wt.% martensite, and 33 wt.% austenite. Both the 600ºC and the 625ºC samples consisted of fine-grained ferrite with mixed martensite/austenite pools. The austenite was subdivided the martensitic matrix. The 625ºC sample was 54 wt.% ferrite, 6 wt.% martensite, and

33 wt.% austenite. The 650ºC and 675ºC samples were 34 wt.% ferrite/ 22.5 wt.% martensite and 20 wt.% ferrite/ 78.6 wt.% martensite, respectively. Blocks of austenite were seen in the 650ºC sample, while minimal amounts of austenite were found in the 675ºC sample. Insufficient grain boundary constraint due to ferrite grain growth (1.5 microns) was a possible explanation for small amounts of austenite in the 650ºC sample [40][20]. Gibbs et al.'s experiments showed austenite mechanical stability depends on the IA temperature.

Lee et al. performed IA experiments from 640ºC to 700ºC for 180 s of a 0.05C-6.15Mn-1.5Si (mass percent) steel [19]. RA volume fraction was found by X-ray diffraction, magnetic saturation, and feritscope measurements. The first two methods showed a reduction in RA from 640ºC to 660ºC; however, the feritscopic measurement showed an increase in RA. Good agreement was found for the 680ºC IA sample of 32% average volume fraction of RA [19]. The volume fraction of RA also increased with IA temperature when the samples were heated at 200ºC and held for 2 s. De Cooman et al.'s experiments included IA at 600ºC and 650ºC for 168 hours of a 0.1C-7.1Mn-0.13Si steel [21]. TEM observation showed the 600ºC sample had coarse carbides in ferrite due to low solubility of C in ferrite. Austenite islands contained stacking faults with small recrystallization twins. No martensite was found in the 600ºC as IA. The dislocation density in ferrite was significantly higher in the 650ºC IA sample, and austenite possessed stacking faults (some partially transformed to α' martensite and ε martensite in athermal manner) [21]. The IA temperature affected the austenite stability and controlled the C/Mn content in RA.

Cai et al. also looked at IA at 730ºC to 850ºC for 3 minutes of a 0.18C–11Mn–3.8Al steel [23]. The as-rolled microstructure showed intercritical ferrite and austenite with layered delta ferrite. Initially, the volume fraction of RA increased from 59% to 69% when IA increased from 730ºC to 800ºC. At an IA of 850ºC, the RA amount was 59% because of unstable austenite

transformation to martensite upon cooling [23]. Austenite stability depended on chemical composition, grain size and morphology. Han et al. investigated a 0.14C–10.2Mn–1.5Al steel subjected to IA at 640ºC from 3 minutes to 48 hours [40]. The mean grain size increased from 201 to 402 nm for austenite and 180 to 326 nm for ferrite. At 12 hours, the area fraction of bigger grains (0.5µm) was higher. The dominant grain size increased from 0.55µm at 3 minutes to 0.95-1.15µm for 12 hours. The martensite reversion transformation resulted in austenite inheriting high dislocation density from parent martensite [40]. A high fraction of substructure was difficult to recover due to slow Mn diffusion rate at shorter IA times, and the growth of austenite grains was shown to reduce stability. No evidence of mechanical twinning found in the 3-min or 12-hr samples with TEM [40]. Acicular and globular austenite were found in the 3-min and 12-hr fractured samples. Co-existence of martensite and austenite in one grain was also observed similar to De Cooman et al.'s experiments [21].

De Cooman et al. performed IA from 850ºC to 1150ºC from 1 s to 240 s [41]. The highest volume fraction of RA for the IA samples was around 50%. Also, Rana et al. applied IA for 16 hours at 640ºC on two similar steels: Fe-10.1Mn-0.14C-0.21Si-1.68Al and 7.4Mn-0.14C-0.21Si-1.55Al [42]. The volume fraction (VF) of RA for each sample was 57.3% and 34.8%, respectively. The as-annealed microstructures had ultra-fine-grained ferrite, austenite, martensite or martensite/austenite islands. Chandan et al. studied prior austenite grain (PAG) size effect on microstructure of an IA medium manganese steel [43]. A 0.3C – 8.1Mn – 1.5Al – 1.1Si – 0.02P – 0.008S steel was heated at 900ºC for 15 minutes and 1000ºC for 20 minutes quenching to develop different PAG sizes before water quenching. Both samples were then IA for 660ºC for 1 hour. The average PAG size was 20.19 and 39.81µm for the 900ºC sample and 1000ºC sample, respectively. The 900ºC sample had an initial austenite volume fraction of 9.8%, and the 1000ºC sample had

6.7%. After IA, the 900ºC sample had 54.4% volume fraction of austenite, and the 1000ºC sample had 39.3%. Both samples contained ultra-fine-grained microstructures with stable austenite films in-between martensite laths. No carbides were seen, as both temperatures were higher than any predicted temperature for carbide formation. Austenite and martensite followed the Kurdjumov – Sachs orientation relationship. The size distribution for austenite films was calculated from 100 austenite films in 20 different TEM micrographs. Austenite thickness was 366 nm for 900ºC sample and 206 nm for 1000ºC sample. The slightly higher VF of austenite in 900ºC sample prior to IA is due to smaller PAG size and lower M_s temperature. This sample has a higher density of martensite laths, which new austenite forms at along with PAG boundaries. The extra nucleation sites for austenite enhances the kinetics of martensite reversion; therefore, the 900ºC sample has a higher VF of retained austenite.

1.5 Mechanical Properties of Quenched and Partitioned Steels

Quenched and partitioned steels have attractive mechanical properties because of their dual phase nature. Retained austenite under deformation can transform to martensite and delay the onset of necking, known as transformation induced plasticity (TRIP). Dislocations are introduced for strain accommodation between martensite and austenite, which increases strain hardening [24]. De Moor et al. performed tension tests at 5.6×10^{-4} /s strain rate on quenched and partitioned steel with varied partitioning temperatures (PT) and partitioning times (Pt). Ultimate tensile strength (UTS) decreased with increasing PT and Pt; however, the yield strength (YS) did not correlate to PT or Pt. Total elongation (TE) increased overall with increasing PT and Pt. Combinations of 800 MPa/25% TE, 900 MPa/20% TE, and 1050 MPa/10% TE were obtained through quenching and partitioning. Strain hardening decreased continuously for the samples partitioning at 350ºC and 400ºC for 60 s Pt, similar to dual phase behavior [24]. The 450ºC sample showed constant strain

hardening which was more representative of TRIP behavior. During strain hardening of 180 s Pt samples, the 400ºC and the 450ºC samples exhibited TRIP behavior. Oscillations in the strain hardening curve were considered dynamic strain aging [20, 38]. Finer grain size of austenite led to higher mechanical stability, and the yielding of these Q&P steels was governed by the yielding of retained austenite [24]. Lis et al. performed tension tests on one-step Q&P steels [3]. A new type of steel was observed with over 2000 MPa UTS and 10% TE. UTS and YS increased until 180 s Pt, then decreased with longer Pts. TE increased with longer Pt correlating to increased VF of RA. De Moor et al. performed mechanical testing on intercritically annealed and fully austenitized Q&P steel [5]. The applied strain rate was 5.6×10^{-4} /s with a 2-inch extensometer attached. UTS ranged from 985 to 1190 MPa for the 0.2C–3Mn–1.6Si grade, 875 to 910 MPa for the 0.3C–3Mn–1.6Si grade, and 1110 to 1175 MPa for the 0.3C–5Mn–1.6Si grade [5]. TE for these grades were 14-20%, 14-18%, and 7-15%, respectively. The YS/UTS ratio increased with increasing additions of C and Mn, and significant strain hardening resulted. UTS decreased and TE increased with increasing PT and Pt [5]. Strain hardening decreased with increasing additions of C and Mn. For the fully austenitized samples, UTS ranged from 1225 to 1450 MPa, 1420 to 1710 MPA, and 690 to 1550 MPa for the three C-Mn-Si grades, respectively. TE was 9-15%, 2 - 17%, and 0.4-14% for the 0.2C–3Mn–1.6Si grade, 0.3C–3Mn–1.6Si grade, and 0.3C–5Mn–1.6Si grade, respectively. The low ductility in the fully austenitized 0.3C–5Mn–1.6Si grade was likely from untempered martensite. The Q&P process for this grade was not optimized [5].

Thomas et al performed uniaxial tension tests on one-step intercritically annealed (IC) or fully austenitized (FA) Q&P steel [26]. Samples were subjected to 2.54 mm/min constant crosshead speed. An 8 mm extensometer was used, and each test was paused at 14% strain, 1% strain before maximum range of extensometer, before resetting the extensometer and continuing

the test. The UTS for the IC samples was insensitive to coiling/quench temperatures above 350ºC and below 225ºC [26]. Between these two temperatures, a transition exists from one plateau to another. The YS increased with increasing coiling/quench temperatures; so, the YS/UTS ratio also increased [26]. Uniform elongation (UE) increased slightly up to 300ºC, then rapidly up to 350ºC. For the FA samples, UTS values ranged from 1100 to 1400 MPa, and TE values were 4-7%. This study focused on IC samples because the higher TE values were present than the FA samples [26]. The IC samples with dual phase microstructures possessed the highest UTS values and lowest YS values. The reason behind these values was high density of mobile dislocations and internal stresses from shear and volume expansion of martensite formed from austenite. Unpinned dislocations around martensite allowed the steel to yield continuously. When the coiling/quench temperature was increased, aging of the ferrite surrounding martensite increased; thus, some dislocations became pinned, and the YS increased [26]. The mechanical properties of the IC samples transformed from dual phase to TRIP mechanical behavior with increasing coiling/quench temperature.

Paravicini et al. performed uniaxial tension tests on different Q&P steels [45]. The UTS was mostly constant (between 1450 and 1500 MPA) with the exception of the sample with the highest quenching temperature (UTS at 1600 MPa). Likely, untempered martensite (UM) was present in this steel. YS values varied between 800 and 1175 MPa, and TE values were 8-14.5%. Additionally, YS and TE had a maximum at 250ºC quench temperature [45]. This temperature coincided with the maximum volume fraction (VF) of retained austenite (RA) and lowest VF of UM. Austenite stability contributed to the YS increase. These Q&P steels had low YS/UTS ratios (0.6-0.7) due to continuous yielding and high work hardening. Dislocations had free mobility, and

RA reduced YS and transformed to martensite. The lowest QT (240-250ºC) samples had YS/UTS ratios of 0.8 with constant yielding and lower work hardening.

Thomas et al. performed tension tests of Q&P steel at constant crosshead speed of 2.86 mm/min until 2% strain, then 22.86 mm/min until failure [46]. An extensometer with gauge length of 50.8 mm was used. Some samples reached a product of strength and elongation (PSE) over 25,000 MPa×%. Figure 1.13 shows the trends of YS, UTS, TE, and UTS×TE with 3 PTs and 4 Pts. The sample fully austenitized at 875ºC for 300 s before water quenching showed very little enrichment of austenite and reached the highest level where tempering phenomenon do not dominate. The maxima for TE at 200ºC and 400ºC PT occur at 100 s and 30 s Pt, respectively. The TE for the 300ºC sample increases sharply after Pt of 0 s, then more gradually up to 1000 s Pt. The maximum PSE was found at 400ºC PT for 30 s Pt and 200ºC PT for 100 s Pt; all Pts above 30 s yielded high PSE values for 300ºC, with 1000 s Pt having the maximum PSE for the study. De Cooman et al. investigated medium manganese steel subjected to intercritical annealing/quenching and partitioning [41]. They performed uniaxial tension tests at 0.001 /s strain rate. The UTS stayed relatively constant (around 1500 MPa), but the YS was inversely proportional to quench temperature (QT). TE peaked at 60ºC then decreased with increasing QT. The 60ºC QT sample had a high YS value due to presence of tempered α' martensite. The transition from elastic to plastic flow was smooth with no serrations apparent in the flow curve [41]. After decreasing sharply, the strain hardening curve remained flat throughout deformation. The true stress-time and true strain-time curves showed strain rate in the Q&P sample was the same as the externally applied strain rate.

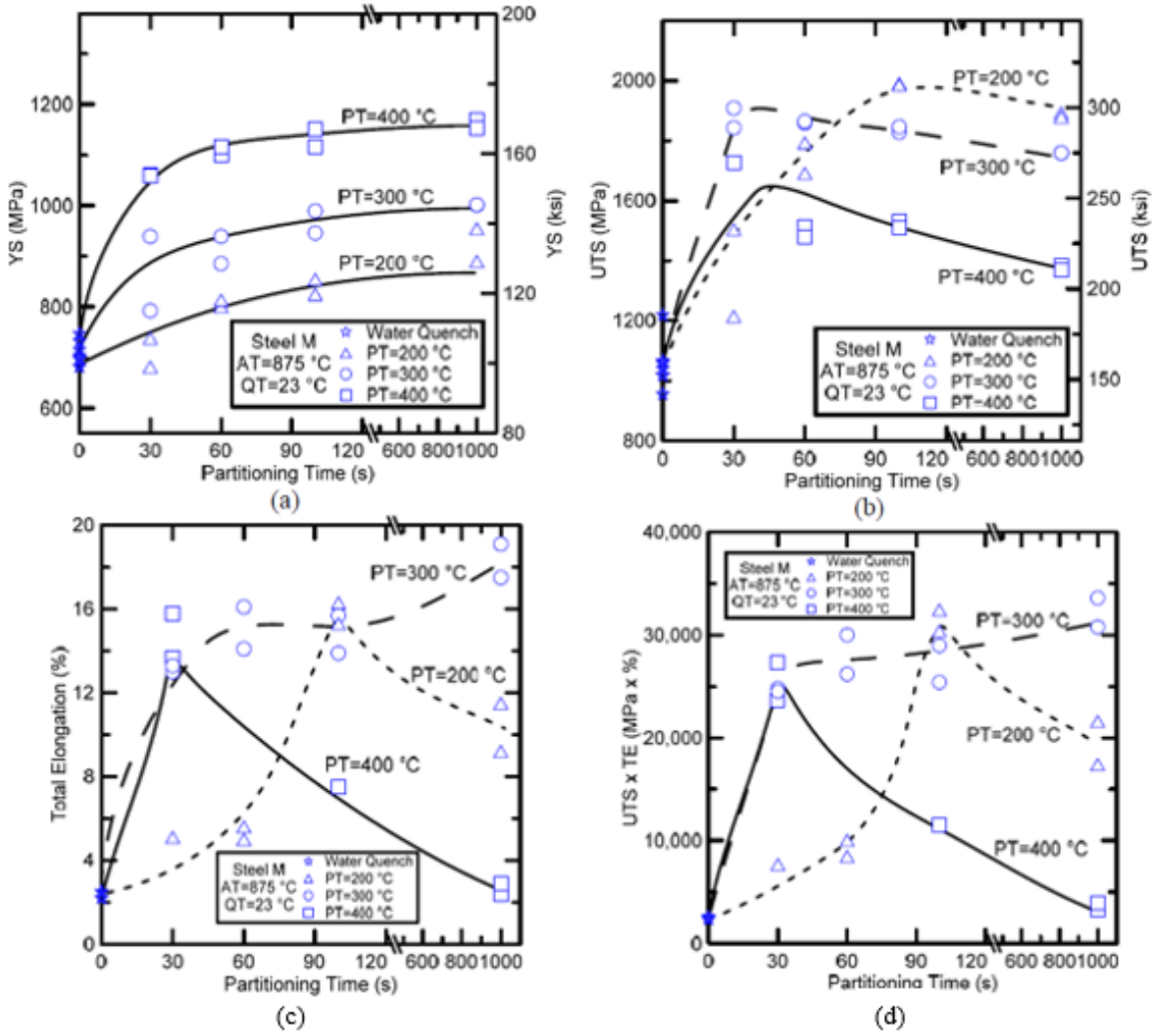

Figure 1.13 Trends of a) YS b) UTS c) TE and d) UTS×TE for medium manganese steel partitioned at 200-400ºC for 0-1000 s [46].

1.6 Mechanical Properties of Medium Manganese Steels

Medium manganese steels have attractive properties in terms of ductility. Their ultra-fine-grained microstructures contain ferrite and highly stable austenite, which delay the TRIP effect and result in yield point elongation with low work hardening. Miller et al. first saw mechanical properties of medium manganese steels subjected to intercritical annealing [12]. The YS values

varied from 600-951 MPa. UTS ranged from 878-1200 MPa, and TE was 12-34%. Similarly, Merwin et al. performed tension tests on medium manganese steel subjected to cold spot and hot spot annealing [38]. The maximum YS was achieved in Alloy 66 with coiling at 538ºC, which exceeded 900 MPa. Alloy 65 and Alloy 64 had around 900 MPa at 538ºC and 732ºC, respectively. Alloy 65 had the highest UTS, exceeding 1200 MPa at 732ºC coiling temperature, while Alloy 64 exhibited the lowest at 750 MPa at 593ºC coiling temperature [38]. Alloy 65 had highest uniform elongation of 32%, and Alloy 64 showed the highest TE at 40%; both properties were at 649ºC coiling temperature. The best product of strength and elongation was found at 649ºC coiling temperature for Alloy 65 exceeding 30,000 MPa×%. Decreasing strength and increasing ductility trended well with increased RA content [38].

Kim et al. performed uniaxial tension tests on three different medium manganese steel alloys [33]. Three different stress-strain curvess for Alloy-1 were observed in Figure 1.14. The 610ºC annealed sample showed large Lüders strains with minimal work hardening. The 640ºC sample showed large Lüders strains and significant work hardening, and the 670ºC sample showed continuous yielding with high work hardening. For the low annealing temperatures (590ºC and 610ºC), UTS decreased with increasing annealing temperature, TE increased. Increasing austenite grain size and lower dislocation density was the cause of these trends [33].

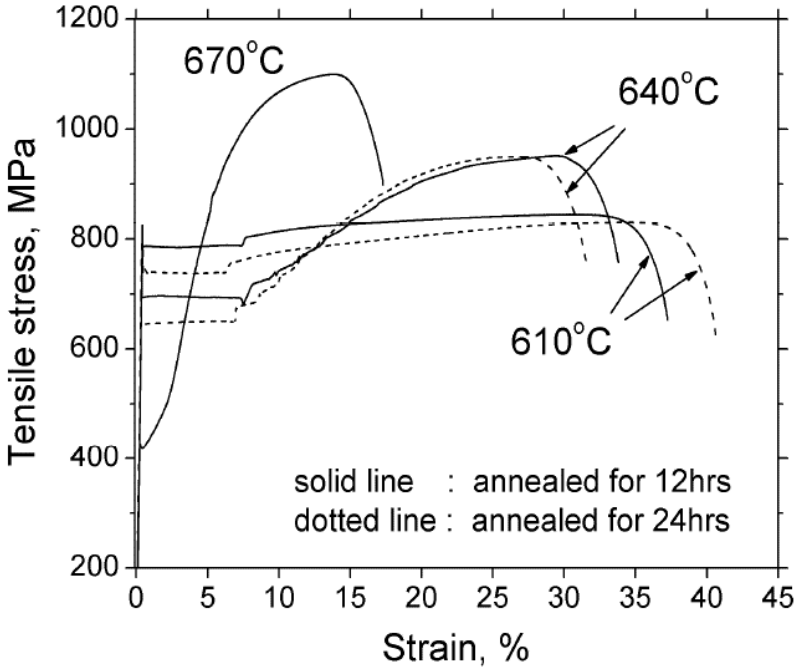

Figure 1.14 Stress-strain curves of Alloy-1 subjected to 610-670ºC IA for 12 hours and 24 hours [33].

For the higher annealing temperatures (640ºC to 670ºC), UTS remained constant, but TE decreased with increasing annealing time. The stability of austenite was lower at these temperatures and more susceptible to martensite transformation. Alloy-2's stress-strain curve is shown in Figure 1.15. The mechanical behavior of three IA samples is similar to Alloy-1 only 760ºC sample exhibited more work hardening than the 610ºC sample. Alloy-2's mechanical properties suggested that a UTS of 1 GPa and TE of 30% was possible given correct optimization. Alloy-3's stress-strain curve is shown in Figure 1.16 for IA temperatures of 600-640ºC. A very high UTS was present (over 1.3 GPa) with TE more than 25%. Jerky or stepwise flow was seen in the stress-strain curves possible from discontinuous martensite formation during deformation [33]. UTS increased with increasing IA temperature, and TE decreased.

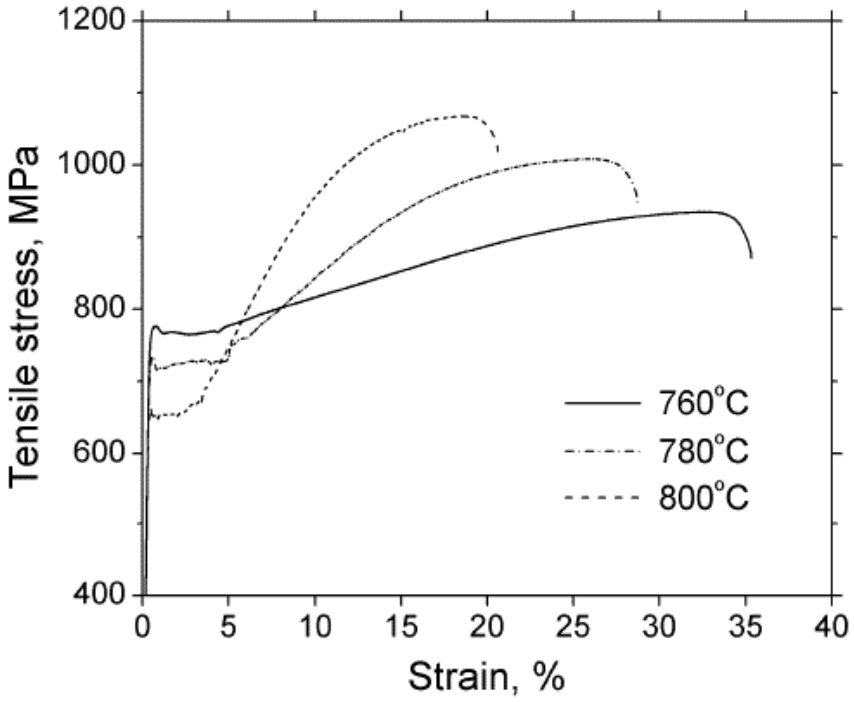

Figure 1.15 Stress-strain curves of Alloy-2 subjected to 760-800ºC IA for 2 minutes [33].

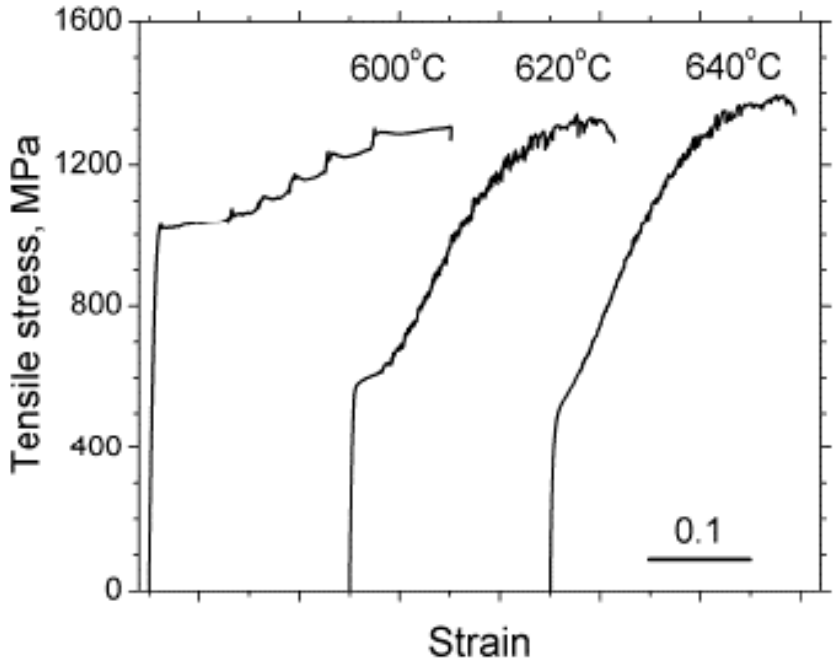

Figure 1.16 Stress-strain curves of Alloy-3 subjected to 600-640ºC IA [33].

Gibbs et al. performed uniaxial tension tests on IA medium manganese samples which were subjected to neutron diffraction [20]. A constant strain rate of 5.74×10^{-4}/s was used on ASTM E8 sub size dog bone samples with 25 mm gage length. Figure 1.17 shows the stress-strain curves for the 575-675ºC IA samples.

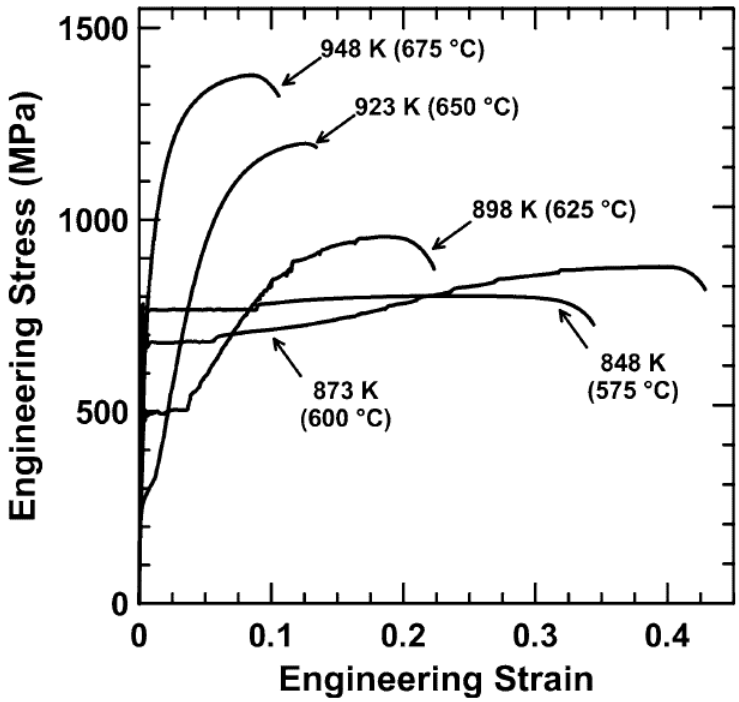

Figure 1.17 Stress-strain curves of samples IA from 575ºC to 675ºC for 168 hours. The 575ºC sample shows the highest austenite stability, but the 600ºC shows the highest ductility.

The 575ºC sample showed the longest yield point elongation (YPE) with limited strain hardening. Very little TRIP occurred, showing that austenite was stable. The TE for 575ºC sample was 35% and the UTS was 800 MPa. The 600ºC sample had a lower YS than the 575ºC sample (around 700 MPa versus 765 MPa) and discontinuous yielding [20]. The 600ºC sample's strain hardening increased causing the UTS to increase (900 MPa). A well-defined YPE existed in 600ºC

sample's curve with signs of ferrite deformation. Serrations in the stress-strain curve were present, and the 600ºC sample displayed the highest TE of 40%. The 625ºC sample had a decrease in YPE and YS (503 MPa), but higher UTS (954 MPa) [20]. The stability of austenite in the 625ºC sample was lower compared to the previous two samples; thus, more austenite transformed to martensite quicker, and the strain hardening increased. The 650ºC sample possessed a higher UTS than the previous samples (around 1200 MPa) and the lowest YS (approximately 270 MPa). No YPE was present, and the stress-strain curve mimicked that of dual phase steels. A strain inflection existed around 0.02 strain, indicating Lüders band propagation with a TE value around 10% [20]. The 675ºC sample exhibited continuous yielding with the highest YS around 770 MPa. The 675ºC sample displayed the highest UTS (about 1368 MPa), but the lowest TE (around 7%). A progressive instability of austenite existed when the IA temperature increased from 600ºC up to 675ºC. In the 625ºC and 650ºC, the largest fractions of retained austenite transformed before the samples reached 8% strain [20]. After 10% strain, 2/3 of the 600ºC sample's austenite transformed, leading to the highest ductility seen in this study.

Lee et al. also performed uniaxial tension tests on IA medium manganese steel at 0.001/s strain rate [19]. Dog bone samples were machined according to the ASTM E8 standard, and an extensometer with 50 mm gage length was used. The 680ºC sample had the maximum work hardening rate. Transformation from austenite to martensite was observed in the grip section of the 680ºC sample. The 640ºC sample exhibited very little work hardening and no transformation from austenite to martensite [19]. The 660ºC sample and 700ºC sample showed austenite transformation to martensite in the gage section only. The Lüders elongation decreased with increasing IA temperature, and no Lüder's elongation was seen in the 700ºC sample. The 680ºC sample showed Lüder's strain with highest work hardening rate. This mechanical behavior

combination resulted in an efficient TRIP effect, where strain induced transformation occurred gradually within the retained austenite [19]. Through infrared (IR) thermography, localized deformation bands were observed in all IA samples. The 640ºC sample had three bands that propagated throughout the gage length, after which, uniform deformation was observed. Two of the bands were recognized as Lüders bands with 66 deg. orientation to the tensile axis [19]. The 660ºC sample had one band propagate, while the 680ºC sample had multiple. The 700ºC showed no localization; therefore, no deformation band was observed. The 640ºC sample had the longest TE, but the 680ºC had the highest mechanical properties overall.

Similarly, De Cooman et al. examined IA medium manganese steel subjected to uniaxial tension testing [21]. ASTM E8 sub size dog bone samples were used along with 5.74×10^{-4}/s strain rate. The 600ºC had a sharp yield point at 700 MPa and discontinuous yielding. Strain hardening from TRIP was present, characterized by spikes in stress after parabolic hardening. The 650ºC sample had lower yield point (around 250 MPa) with very little work hardening, mostly parabolic [21]. Strain hardening decreased with strain for the 650ºC sample. There were many instabilities in 600ºC sample's flow curve; whereas, the 650ºC sample exhibited homogeneous plastic deformation. Significant austenite transformation occurred from 250 to 400 MPa and 650 to 800 MPa for the 650ºC and 600ºC sample, respectively. The 650ºC sample experienced rapid stress-assisted austenite transformation and decreased strain hardening, while the 600ºC sample had a constant transformation rate due to fully recrystallized ferrite and austenite grains [21]. De Cooman et al. defined a range between stress-assisted and strain induced transformation to austenite based on martensite start (M_S) temperature. In the $M_S^\sigma - M_s$ regime, martensite nucleation occurred on existing sites, enhanced by stress. In the $M_S^\sigma - M_d$, martensite formation occurred on sites made by plastic deformation, such as slip bands. For the 600ºC, most of

martensite formation occurred in the $M_S^\sigma - M_d$ range, while the 650ºC had most martensite formation in the $M_S^\sigma - M_s$ range.

Gibbs et al. also studied medium manganese IA at 600ºC and 650ºC [22]. Uniaxial tension tests were performed at 5.74×10^{-4}/s strain rate on ASTM E8 sub size dog bone samples with a 25.4 mm extensometer. Neutron diffraction was used during deformation to track phase evolution during deformation. The 600ºC sample had a YS of 685 MPa, UTS of 870 MPa, and TE of 41.5% [22]. The 650ºC sample possessed a YS of 250 MPa, UTS of 1200 MPA, and a TE of 10%. Discontinuous yielding was present in the 600ºC sample along with a Lüders plateau. The 650ºC sample exhibited a pronounced inflection in the stress-strain curve. A positive slope of work hardening was observed in both samples during deformation, signifying a TRIP effect. The amounts of α' martensite and ε martensite rapidly increased after the 650ºC sample yielded [22]. Overall, the martensite fraction increased until the amount of austenite transformed was 92%. Grain orientation did not influence the degree of transformation. In the 600ºC sample, α' martensite and ε martensite did not appear until the end of yield point elongation. Orientation of austenite dependence was observed as the $\gamma_{[220]}$ planes decreasing more rapidly than the $\gamma_{[311]}$ planes [22]. Three distinct stages were observed in the lattice strain date for the IA samples. Stage 1 was initial linear and reversible deformation as the strains were tensile in the axial direction and compressive in the transverse direction. Stage 1 occurred in the 600ºC sample and the 650ºC sample but ended at different stress levels. Abrupt compression during yielding in the axial and transverse direction for austenite signified Stage 2. Stage 2 occurred at 685 MPa (macroscopic yield), where the ferrite and austenite strains diverged. Lattice compression was seen in the axial and transverse direction for austenite. For the 650ºC, Stage 2 happened at 330 MPa. The compressive strains for austenite were lower than the 600ºC sample. Lastly, Stage 3 was the arrest of lattice strain in the ferrite axial

direction and occurred at 730 MPa and 700 MPa for the 600ºC and 650ºC sample, respectively [22]. Stress-assisted mechanisms for austenite transformation to martensite were present in the 650ºC sample. Low stability from low Mn enrichment led to more transformation early during straining and increasing work hardening rate. In contrast, strain-induced mechanisms occurred in 600ºC sample's austenite due to high austenite stability from high C and Mn enrichment [22].

Likewise, Cai et al. performed uniaxial tension tests on IA medium manganese samples [23]. A gage length of 25 mm was used along with constant crosshead speed of 3 mm/min. The UTS increased with increasing IA temperature. A TE maximum of 70% was found at 750ºC IA temperature, then TE decreased with increasing IA temperature. A linear decrease in YS was observed consistent with increasing grain size following the Hall-Petch relationship [23]. The 770ºC sample exhibited the best mechanical properties with UTS of 1007 MPa and TE of 65%. The PSE value was equal to 66GPA×%. The 730ºC sample and 800ºC sample had austenite transformation ratios of 35% and 76%, respectively; therefore, the 730ºC sample had the highest austenite stability of the three IA samples, but lower UTS (875 MPa). The 800ºC sample had a UTS of 1087 MPa. The TE values for the 730ºC sample and 800ºC sample, however, were very similar (45% versus 43%)[23]. Ductility in the 730ºC sample was from ferrite deformation, while the 800ºC sample's ductility came from the TRIP effect. Sufficient austenite stability was needed to prolong TRIP and enhance ductility. The work hardening behavior for the IA samples is depicted in Figure 1.18. In the 730ºC sample, Stage 1 work hardening decreased monotonically to lowest value of the three IA samples [23]. Stage 1 for both the 770ºC and the 800ºC samples also decreased. In Stage 2, the 730ºC sample continued to show decreasing work hardening but a less severe rate than Stage 1. This slowed rate was due the TRIP effect occurring simultaneously with ferrite deformation.

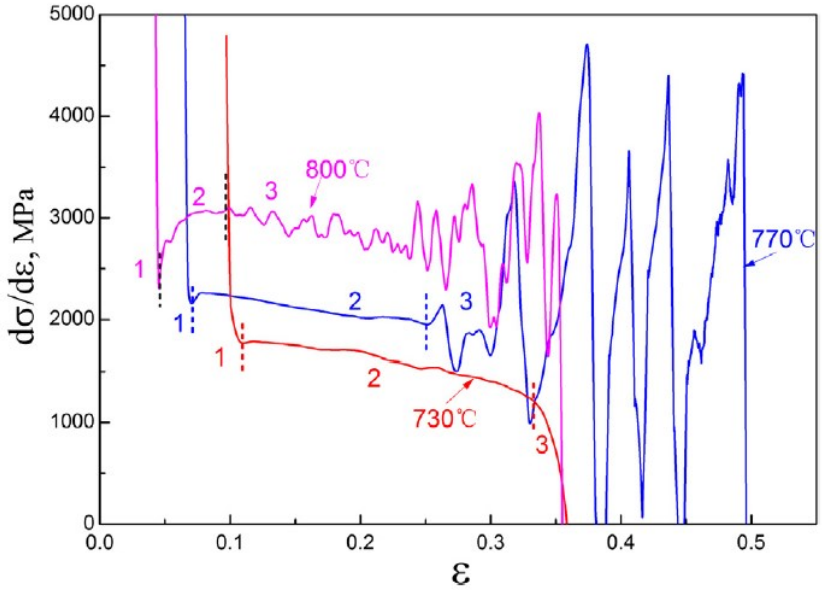

Figure 1.18 Work hardening rates versus strain for 730-800ºC IA samples showing Stages 1-3 [23].

Stage 2 for the 770ºC sample is similar to the 730ºC sample only at a more gradual rate. Stage 2 for 800ºC sample is more constant than the previous samples. Stage 3 for the 730ºC sample is a sharp decrease in work hardening. For the 770ºC sample, Stage 3 is similar to Stage 3 for the 800ºC sample, only the work hardening fluctuates significantly due to a discontinuous TRIP effect. The large fluctuations result in enhanced strength and ductility [23].

Using IA medium manganese samples, Rana et al. performed tension tests at different test temperatures and strain rates to explore adiabatic heating effect on austenite stability [47]. ASTM E8 sub size dog bones were used along with a 25.4 mm gage length extensometer. Samples were submersed in ethanol from -100-20ºC and in oil from 60-100ºC. Tensile tests were additionally performed in air as comparison to liquid effect on adiabatic heating. A K-type thermocouple was welded on the surface to monitor temperature changes during the test [47]. The resulting martensite fraction was higher in the -60ºC test than the 100ºC test, showing a temperature dependence on

the TRIP effect. The austenite transformation ratio increased with test temperature independent of strain rate. Austenite stability also increased, and at low temperatures (-60 to 20ºC), was very similar for the two medium manganese steels. At higher temperatures (60 to 100ºC), the 10MnAl steel had higher austenite stability than the 7MnAl [47]. The strain hardening rate inversely proportional to test temperature as the austenite stability diminished. The UTS for both steels decreased with increasing test temperature independent of the strain rate (Figure 1.19). The 7MnAl sample possessed lower UTS values than the 10MnAl, which had a higher initial volume fraction of retained austenite. More transformation occurred in the 10MnAl leading to a higher strain hardening, and more pronounced TRIP effect. Adiabatic heating is shown to increase austenite stability and decrease UTS in the strain rates performed in this study. A negative strain rate sensitivity is observed from 0.002 to 0.2/s strain rate because of adiabatic heating.

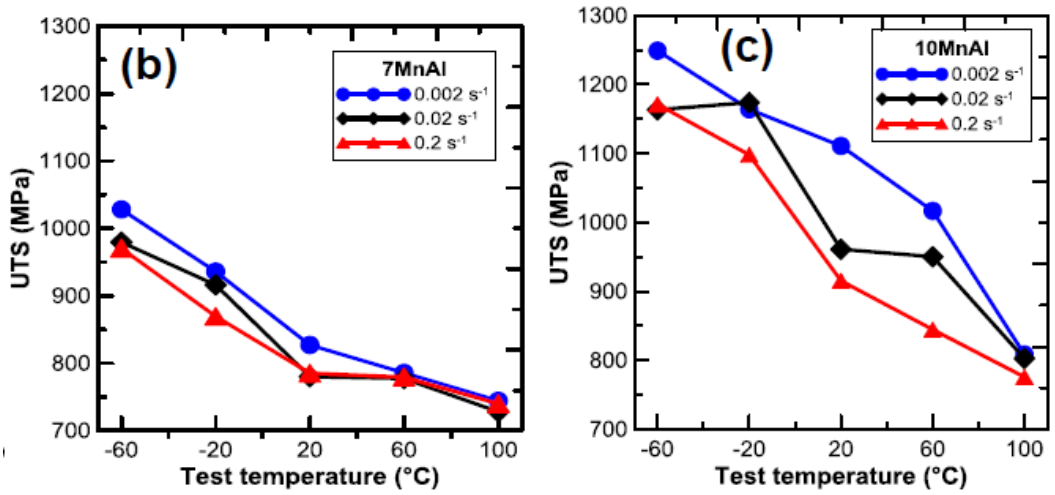

Figure 1.19 UTS value versus test temperature at three strain rates for a) 7MnAl and b) 10MnAl.

Likewise, Dutta et al. performed uniaxial tension tests on IA medium manganese steel at 0.001/s strain rate [48]. A 4 mm gage length sample was used along with in-situ EBSD. The cold-rolled (CR) and hot-rolled (HR) IA steel experienced continuous yielding. Figure 1.20 shows the stress-strain curves and volume fractions of martensite/retained austenite for the CR and HR material. The CR material had a higher YS (625 MPa versus 520 MPa) and a higher UTS (773 MPa versus 690 MPa) than the HR material. However, the HR material possessed a longer TE than the CR material (18.5% versus 15.5%) [48]. The volume fraction of austenite in the HR material was initially 34% from EBSD, then decreased to 24% near necking. The CR material exhibited a volume fraction of 26% initially that decreased to 19% near necking. Austenite began to transform at 2% engineering strain for the HR material and at 11% for the CR material. The CR material exhibited more continuous yielding between 2-5% engineering strain.

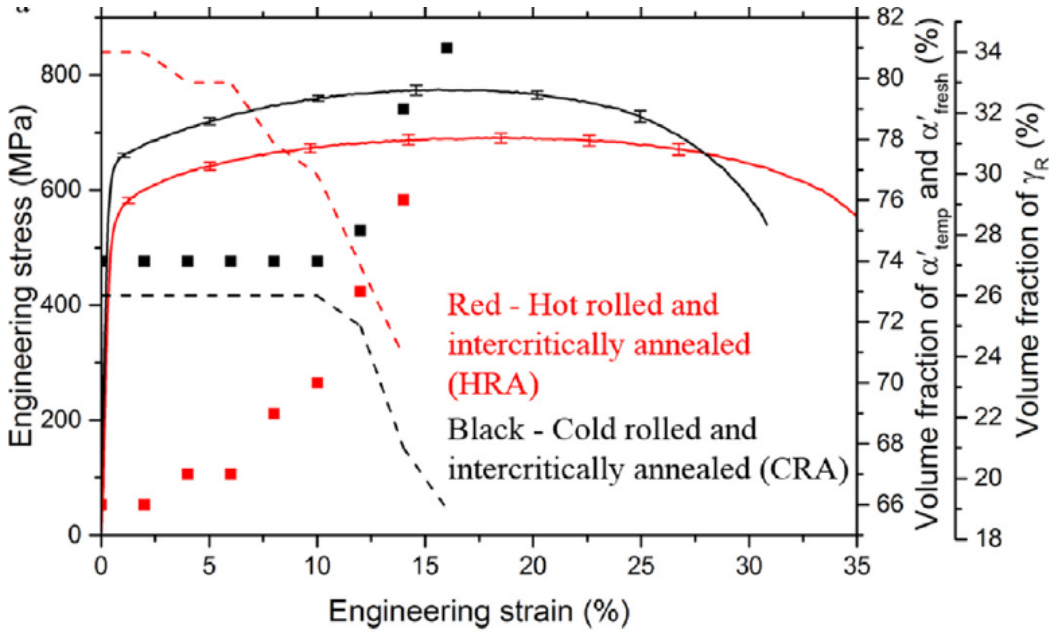

Figure 1.20 Stress-strain curves for the CR and HR material along with volume fractions of martensite and retained austenite.

The deformation of the HR material is complex because strain was partitioned between different phases. Higher local von Mises strain of 15% was present in the retained austenite/untempered martensite region at 7.1% global strain compared to tempered martensite, which had less than 5% [48]. The local von Mises strain was concentrated in the softer retained austenite islands during early stages of yielding. The global strain above 10% is accommodated by the retained austenite islands and tempered martensite. For the CR material, a local von Mises strain of 10% was present in the retained austenite/untempered martensite region at 5% global strain compared to tempered martensite, which had less than 5%. Above 5% global strain, the local von Mise strain in tempered martensite increases. The strain in the retained austenite results from dislocation slip and twinning, but also shape distortion from transformation to martensite. However, no reduction in austenite volume fraction was detected before 10% global strain; therefore, the strain was dominated by dislocation slip up to global strain of 10%.

CHAPTER II

EXPERIMENTAL PROCEDURE

2.1 TRIP Composition for Quenching and Partitioning

We examined eight different Fe-C-Mn-Si transformation induced plasticity (TRIP) compositions with small additions of Cr/Mo and to a lesser extent of Nb [49]. Manganese is a well-known austenite stabilizer, but also expensive. The maximum limit for Mn was 3.00 wt.%. Carbon is a much cheaper austenite stabilizer; however, too much C will negatively affect weldability, so a 0.30 wt.% limit was set. Silicon is a known cementite suppressant but too much can decrease wettability. A limit of 1.50 wt.% Si was set. Chromium and molybdenum are known austenite stabilizers and add corrosion resistance. Nb promotes grain refinement and precipitation strengthening. Table 2.1 shows the eight selected compositions. Ingots 25 mm thick were cast in a vacuum induction melt furnace at Mississippi State University (MSU), then sent to CANMET at University of Waterloo and hot rolled to a 2 mm thickness before water quenching [49]. The sheets' composition was analyzed at Steel Dynamics Institute (SDI). Table 2.1 shows the target composition and the SDI measurement and acceptable agreement exists between these values. Out of the eight compositions, Comp-2 and Comp-5 were selected for quenching and partitioning (shown in Table 2.2). The two compositions displayed a similar C wt.% and only differed by 1 wt.% of Mn [49]. The remaining compositions will be explored by future graduate students.

Table 2.1 Eight TRIP composition measurements by SDI compared with target values [49].

(wt.%)

Comp	Measure	C	Si	Mn	P	S	Cr	Mo	Nb
1	Target	0.218	1.50	2.85	0.0028	0.0081	0.0260	0.314	0.0327
	SDI	0.200	1.50	3.00	-	-	-	0.300	0.0300
2	Target	0.234	1.47	1.98	0.0020	0.0070	0.0188	0.309	0.0285
	SDI	0.250	1.50	2.00	-	-	-	0.300	0.0300
3	Target	0.227	1.53	2.93	0.0020	0.0063	0.519	0.0039	0.0285
	SDI	0.250	1.50	3.00	-	-	0.500	0.000	0.0300
4	Target	0.252	1.85	1.97	0.0028	0.0073	0.501	0.308	0.0311
	SDI	0.250	1.50	2.00	-	-	0.500	0.300	0.0300
5	Target	0.262	1.44	2.90	0.0020	0.0069	0.0225	0.296	0.0274
	SDI	0.250	1.50	3.00	-	-	-	0.300	0.0300
6	Target	0.216	1.62	2.24	0.0019	0.0060	0.0198	0.322	0.0312
	SDI	0.200	1.50	2.00	-	-	-	0.300	0.0300
7	Target	0.408	1.56	2.18	0.0023	0.0072	0.0201	0.324	0.0302
	SDI	0.300	1.50	2.00	-	-	-	0.300	0.0300
8	Target	0.217	1.48	2.11	0.0018	0.0056	0.493	0.014	0.0240
	SDI	0.250	1.50	2.00	-	-	0.500	-	0.0300

Table 2.2 Two chosen TRIP compositions used in this study [49].

(wt.%)

Sample	Composition
Comp-2	0.234C-1.47Si-1.98Mn-0.019Cr-0.309Mo-0.0285Nb
Comp-5	0.262C-1.44Si-2.90Mn-0.022Cr-0.296Mo-0.0274Nb

2.2 Medium Manganese Composition for Quenching and Partitioning

We chose a composition developed by Thomas et al. to investigate partitioning effects close to martensitic finish (M_f) temperature [46, 50]. A 25 mm thick ingot was cast in a vacuum induction melt furnace at Mississippi State University (MSU). Composition measurements (Table 2.3) were taken from the ingot. Chemical analysis was performed at CAVS with a Spectromax spectrometer and LECO Carbon/Sulfur analyzer [50]. After composition verification, the ingot

was placed in a reheat furnace at 1250ºC for 2 hours, before hot-rolling to 2.5 mm final thickness with a FENN pilot scale rolling mill at MSU.

Table 2.3 Medium manganese steel composition based on Thomas et al.'s experiments [46]. Target values are listed above the CAVS measurements [50].

(wt.%)

Chem	Measurement	C	Si	Mn	P	S	Mo
2-A	Target	0.30	1.50	8.00	-	-	0.25
	CAVS	0.331	1.316	8.212	0.0114	0.00370	0.2038

2.3 Medium Manganese Composition for Intercritical Annealing

The third composition investigated was a medium manganese steel similar to Gibbs et al.'s composition [20, 51]. A 25 mm thick ingots were cast in a vacuum induction melt furnace at Mississippi State University. Composition measurements were taken from the ingot (shown in Table 2.4), and chemical analysis was performed at CAVS with a Spectromax mass spectrometer and LECO Carbon/Sulfur analyzer [51]. After verifying the composition, the ingots were place in a reheat furnace at 1250ºC for 2 hours, then hot-rolled in FENN pilot scale rolling mill at MSU to 4 mm final thickness. After the hot-rolled plates cooled to room temperature, they were cold-rolled to 1.5 mm thickness in the FENN rolling mill [51].

Table 2.4 Medium manganese composition based on Gibb et al.'s experiments [20]. Target values are listed above the CAVS measurements [51].

(wt.%)

Chem	Measurement	C	Si	Mn	P	S
1-A	Target	0.10	0.13	7.00	-	-
	CAVS	0.168	0.134	7.172	0.0118	0.00516

2.4 Sample Geometry for Heat Treatment and Mechanical Testing

The sheets were water jet cut into ASTM E8 sub size tension samples at Tombigbee Tooling Inc [49]. Figure 2.1 shows the A unique feature is the pin holes located within the grip sections to allow placement in the Gleeble grips and Instron grips. Three samples from each composition were pickled in distilled vinegar for 12 hours to remove mill scale before heat treatment in a Gleeble 3500 thermo-mechanical simulator. One sample was used for EBSD and hardness testing, while the other two were for tension testing [49].

Figure 2.1 ASTM E8 sub size dog bone sample for Gleeble heat-treatment and Instron tension testing [49].

2.5 Quenching and Partitioning Heat Treatment I

The critical temperature, A_3, for both steel compositions was 822ºC and 792ºC, respectively. These temperatures were calculated using JmatPro software and to ensure full austenization, 900ºC was selected as austenitizing temperature [49]. The quench temperature, 250ºC, was selected below the M_s temperature for Comp-2 and Comp-5, which were 320ºC and 282ºC, respectively, according to JMatPro. To possibly upscale the heat treatment process of our compositions, the partitioning temperature was selected based on typical temperatures of zinc baths (450-460ºC) used in the production of galvanized steels [52]. Each sample was subjected to the heat treatment profile (Figure 2.2) using a Gleeble 3500 thermo-mechanical simulator [49].

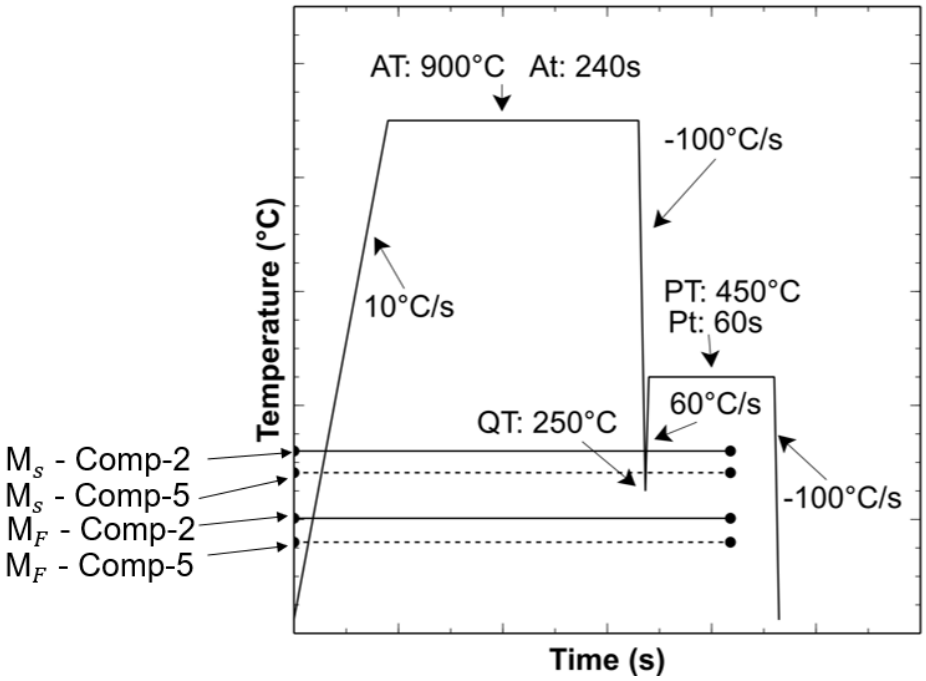

Figure 2.2 Schematic quenching and partitioning applied to lean TRIP composition. AT is austenitizing temperature, At is austenitizing time, QT is quench temperature, PT is partitioning temperature, Pt is partitioning time. Ms is martensite start temperature, and Mf is martensite finish temperature [49].

Each dog bone sample had three thermocouple pairs welded to the surface: one for control in the middle of gage length, and two for monitoring temperature at the gage length ends. Samples were heated in a vacuum (10-8 torr) at 10ºC/s to 900ºC and held isothermally for 240 s, then air quenched at 100ºC/s to 250ºC and reheated at 60ºC/s to 450ºC and held for 60 s, before air quenching at 100ºC/s to room temperature [49].

2.6 Quenching and Partitioning Heat Treatment II (Future Work)

Similar to Thomas et al.'s heat treatment, we will apply quenching and partitioning following the profile in Figure 2.3 [46]. First, the hot-rolled sheets will be water jet cut into ASTM E8 sub size tension samples at CAVS using a Maxiem system [50]. Pin holes will be included in the grip sections to accommodate Gleeble grips for heat treatment. Three K-type thermocouples will be welded on the samples surface within the gage length to control and monitor the temperature. Samples will be heated at 7ºC/s to 875ºC and held isothermally for 300 s before water quenching to room temperature. Samples 1-6 will receive liquid nitrogen quenching to -20ºC, -40ºC, or -60ºC, and samples 7-12 will be reheated to 300ºC at 5ºC/s and held for 60 s before water quenching to room temperature [50].

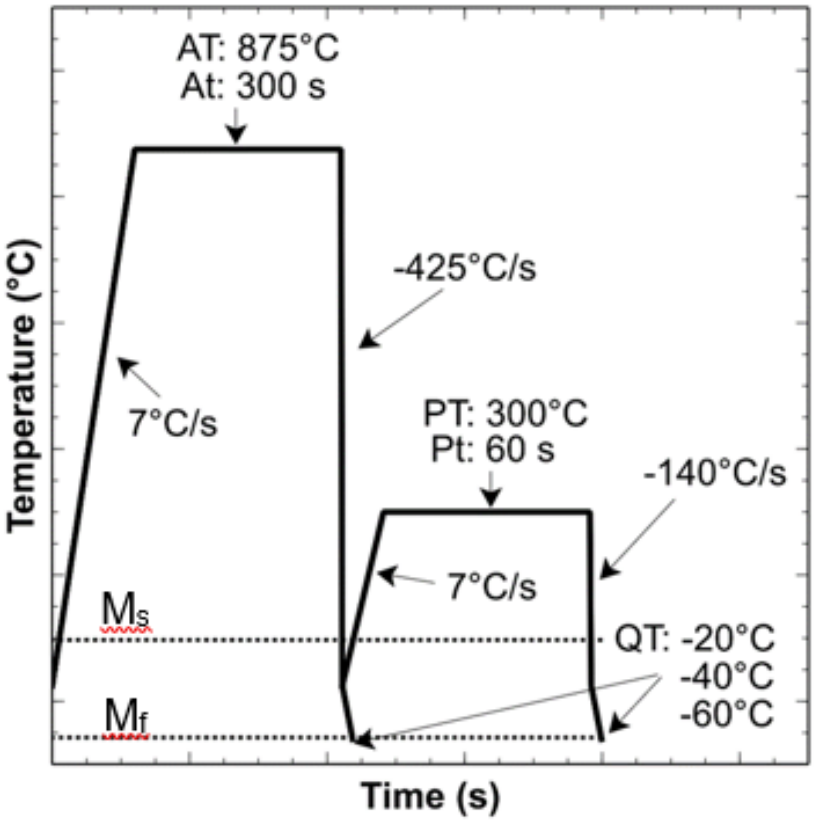

Figure 2.3 Quenching and partitioning heat treatment following Thomas et al.'s experiments [46]. AT is austenitizing temperature, At is austenitizing time, QT is quench temperature, PT is partitioning temperature, Pt is partitioning time. Ms is martensite start temperature, and Mf is martensite finish temperature [50].

Samples 7-12 will then be quenched in liquid nitrogen to -20ºC, -40ºC, or -60ºC. The heat treatment at 875ºC and 300ºC will occur in a helium environment to prevent oxidation [50]. The liquid nitrogen quenching will be performed outside the Gleeble in open air. Samples will be first blown with compressed air to remove any water, then quenched in liquid nitrogen until the quench temperature is reached, then placed in open air until room temperature is reached.

2.7 Intercritical Annealing Heat Treatment I (Future Work)

Intercritical annealing (IA) will be performed similar to Gibbs et al. to confirm mechanical properties [20]. First, the sheets will be water jet cut into ASTM E8 sub size tension samples at CAVS using a Maxiem water jet system. The samples will contain a 1% taper in accordance with ASTM E8 from the gage length end to the center to facilitate failure within the gage length [51]. Four samples (two at each temperature) will be IA for 168 hours (1 week) at 600ºC and 650ºC in Lucifer muffle furnaces in argon atmosphere. At the end of 168 hours, each sample will water quenched to room temperature [51].

2.8 Intercritical Annealing Heat Treatment II (Future Work)

Three periodic intercritical annealing were designed shown by the schematic in Figure 2.4 [51]. Samples will be heat-treated in a Gleeble 3500 thermo-mechanical simulator at 5ºC/s to 575ºC or 625ºC and held for 23 hours. Next, the temperature will be increased to either 625ºC or 675ºC, followed by cooling to 575ºC or 625ºC within 1 hour following Equation 2.1 where, A is the holding temperature for 23 hours (575ºC or 625ºC), B is the amplitude of temperature increase (50ºC or 100ºC), and t is time in seconds [51]. After each 23 hours isothermal hold and 1 hour temperature peak, the thermal cycle will be repeated until 7 cycles have occurred. Then, the sample will be water quenched to room temperature. Two samples will be stacked on top of each other within the Gleeble grips to heat-treat them at the same time. The top and bottom sample each have a thermocouple welded to the surface [51]. The top thermocouple will monitor the temperature, while the bottom thermocouple will control the test. Each test will be performed in a helium environment to prevent oxidation.

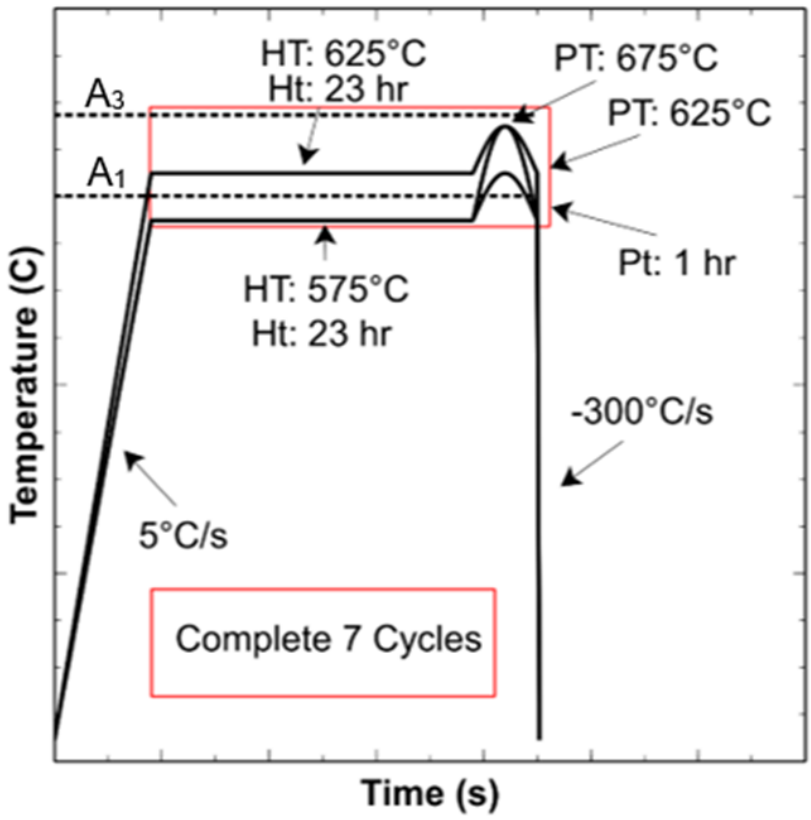

Figure 2.4 Schematic showing periodic intercritical annealing with hold temperatures of 575ºC and 625ºC and peak temperatures of 625ºC and 675ºC. A1 is the critical temperature where austenite begins to form. A3 is the critical temperature above which the microstructure is fully austenitic [51].

$$A + B * \sin\left(\frac{\pi * t}{60}\right) \tag{2.1}$$

2.9 Hardness Testing on Comp-2 and Comp-5

Hardness tests were performed on Comp-2 and Comp-5 for the as-quenched and quenched and partitioned conditions [49]. Samples were ground with 120, 320, 800, 1200, and 2000 grit SiC paper prior to testing. A LECO Rockwell Type Hardness Tester was used, and three measurements were taken in four locations shown by Figure 2.5

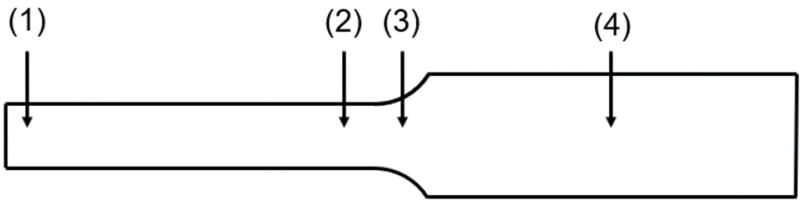

Figure 2.5 Schematic of hardness measurements taken from (1) middle gage length, (2) end of gage length, (3) transition to grip section, and (4) grip section [49].

2.10 Uniaxial Tension Testing for Comp-2 and Comp-5

Mechanical testing was performed at constant crosshead speed (0.0254 mm/s) until failure for Comp-2 and Comp-5 samples [49]. We used an Instron 5900R-5882 load frame and recorded the strain through a low speed camera and digital image correlation (DIC) from Correlated Solutions. Samples were painted with white spray paint, then speckled coated with black spray paint to provide points of reference for DIC strain calculation. Two dots were placed with a Sharpie marker to indicate a 1-inch gage length [49]. All samples broke within the gage length. Each test was duplicated to ensure good repeatability. Yield stress was determined using the 0.02% offset method, and ultimate strength was measured at the endpoint of uniform elongation before necking.

2.11 Uniaxial Tension Testing for Chem-2A

Mechanical testing will be performed at constant crosshead speed (0.0254 mm/s) until failure for Chem-2A samples [50]. We will use an Instron 5900R-5882 load frame and record the strain through a low speed camera and digital image correlation (DIC) from Correlated Solutions. Samples will be painted with white spray paint, then speckled coated with black spray paint to provide points of reference for DIC strain calculation. Two dots will be placed with a Sharpie marker to indicate a 1-inch gage length. Each test will be duplicated to ensure good repeatability.

Yield stress will be determined using the 0.02% offset method, and ultimate strength will be measured at the endpoint of uniform elongation before necking [50].

2.12 Uniaxial Tension Testing for Chem-1A

Mechanical testing will be performed at constant crosshead speed (0.0254 mm/s) until failure for Chem-1A samples [51]. We will use an Instron 5900R-5882 load frame and record the strain through a low speed camera and digital image correlation (DIC) from Correlated Solutions. Samples will be painted with white spray paint, then speckled coated with black spray paint to provide points of reference for DIC strain calculation. Two dots will be placed with a Sharpie marker to indicate a 1-inch gage length [51]. Each test will be duplicated to ensure good repeatability. Yield stress will be determined using the 0.02% offset method, and ultimate strength will be measured at the endpoint of uniform elongation before necking.

2.13 Electron Backscatter Diffraction (EBSD) for Comp-2 and Comp-5

Samples were prepared for EBSD by grinding with 220 grit silicon carbide paper, then polishing with 9 μm and 3 μm diamond slurries [49]. The final two steps were a 0.2 μm OPU solution and 0.05 μm colloidal suspension. EBSD was performed using an EDAX TSL detector within a Supra 40 field emission gun scanning electron microscope (FEG-SEM) was also conducted on the heat-treated gage length to analyze the phase fractions in the microstructure. The working distance was 13 mm, and the scanned area was 30 by 30μm at 50 nm step size. EBSD was performed on the as-quenched material for Comp-2 and Comp-5, and the quenched and partitioned Comp-2 and Comp-5 [49].

2.14 Electron Backscatter Diffraction (EBSD) for Chem-2A (Future Work)

For Chem-2A, 6 samples (one for each heat treatment) will be first austenitized at 875ºC then water quenched [50]. Samples will be ground with 220 grit silicon carbide paper, then polished with 9 μm and 3 μm diamond slurries. The final two steps are polishing with a 0.2 μm OPU solution and 0.05 μm colloidal suspension. After polishing the samples, a small indent will be placed in each sample's gage length, and EBSD will be performed near the indent. EBSD will be performed using an EDAX TSL detector within a Supra 40 field emission gun scanning electron microscope (FEG-SEM). After the first EBSD scan, samples will either be quenched in liquid nitrogen or partitioned/quenched in liquid nitrogen. Samples will be repolished only with 0.2 μm OPU solution and 0.05 μm colloidal suspension, and a second EBSD will be performed in the same location as the first scan. Both scans will be 30 by 30 μm at 13 mm working distance and 50nm step size [50].

2.15 Electron Backscatter Diffraction (EBSD) for Chem-1A (Future Work)

For Chem-1A, samples will be polished following the same procedure for Comp-2 and Comp-5, before and after receiving periodic intercritical annealing [51]. Samples will be ground with 220 grit silicon carbide paper, then polished with 9 μm and 3 μm diamond slurries. The final two steps are polishing with a 0.2 μm OPU solution and 0.05 μm colloidal suspension. EBSD on the heat-treated gage length will be performed using an EDAX TSL detector to analyze the phase fractions in the microstructure. EBSD will be performed using an EDAX TSL detector within a Supra 40 field emission gun scanning electron microscope (FEG-SEM). The working distance will be 13 mm, and the scanned area will be 30 by 30μm at 50 nm step size [51].

CHAPTER III

RESULTS AND DISCUSSION

3.1 Quenching and Partitioning in Gleeble 3500 Results

Figure 3.1 shows the setpoint and actual temperature achieved in the Gleeble 3500 [49]. Very little overshoot or undershoot is observed for the middle thermocouple, while the left and right thermocouples are below the setpoint temperature. The cause of this discrepancy is the continuous cooling of the Gleeble grips during the test. In the partitioning stage, edge cooling is observed as both left and right thermocouples (TCs) slowly drop in temperature [49]. The greatest temperature difference for Comp-2 during austenitization and partitioning is roughly 55ºC and 40ºC, respectively. The left and right TCs were located the furthest from the gage length middle, meaning temperature was higher when measured between the gage length ends and middle. Also, the austenization temps for left and right TCs were 35ºC and 55ºC above the A_3 temperature for Comp-2 and Comp-5, respectively. Austenite grain sizes were likely larger in Comp-5 because of the larger temperature difference [49].

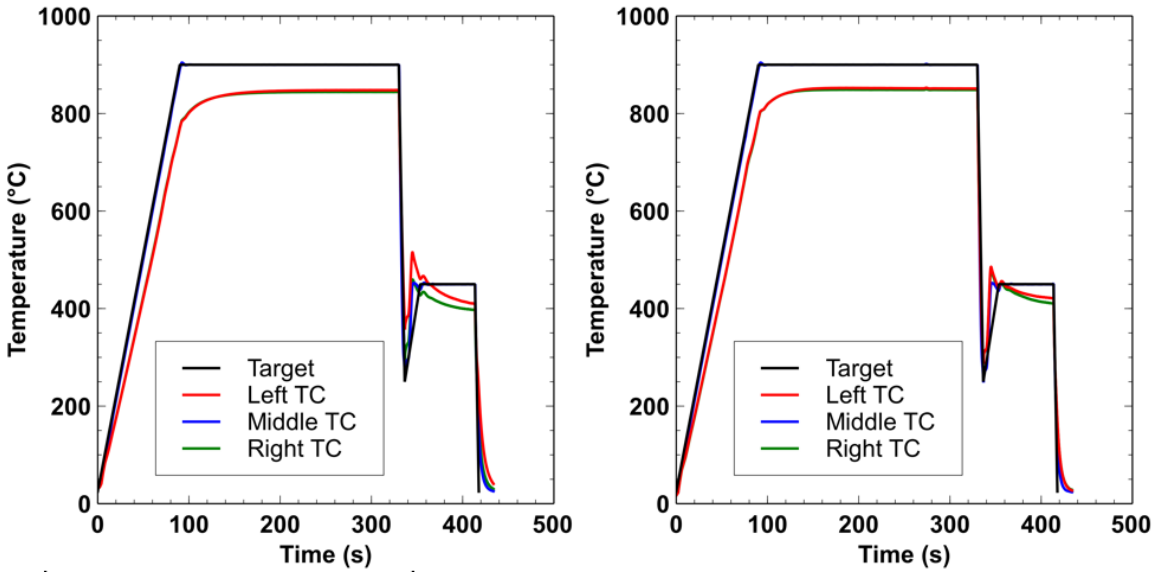

Figure 3.1 Heat treatment profile achieved in Gleeble 3500. The target temperature is the black line while the left, middle, and right thermocouples are the red, blue, and green lines, respectively [49].

3.2 Hot-Rolled and Quenched TRIP Steel Mechanical Results

Comp-2 and Comp-5 had an average Rockwell C hardness of 51.0 ± 0.5 and 47.4 ± 1.0, respectively (Table 3.1) [49]. Figure 3.2 shows the location of hardness tests performed on dog bone samples of Comp-2 and Comp-5. The hardness tests indicated Comp-2 and Comp-5 both were processed homogenously through hot-rolling and water quenching. The as received material had very high strength and low ductility [49].

Table 3.1 Rockwell C-scale hardness values from four locations on dog bone samples of Comp-2 and Comp-5 [49].

Sample	(1)	(2)	(3)	(4)	Average
Comp-2 As Received	50.9 ± 0.2	50.6 ± 0.4	51.3 ± 0.6	51.2 ± 0.5	51.0 ± 0.5
Comp-5 As Received	46.6 ± 1.6	47.5 ± 0.3	47.6 ± 0.3	48.1± 0.7	47.4 ± 1.0

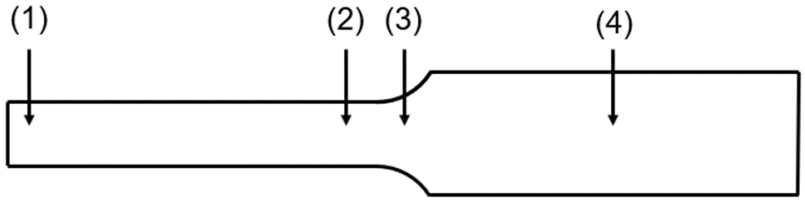

Figure 3.2 Location of hardness tests performed on ASTM E8 dog bone samples of Comp-2 and Comp-5 [49].

Figure 3.3 shows the stress-strain curve of Comp-2 and Comp-5 under constant crosshead speed of 0.0254 mm/s [49]. The mechanical properties for Comp-2 and Comp-5 are in Table 3.2. Comp-5 showed higher ultimate tensile strength than Comp-2 (1923 MPa versus 1844 MPa), but Comp-5 had a slightly higher yield strength (1370 MPa versus 1364 MPa). Comp-2 also had a higher total elongation compared to Comp-5 (7.60% versus 4.00%) [49].

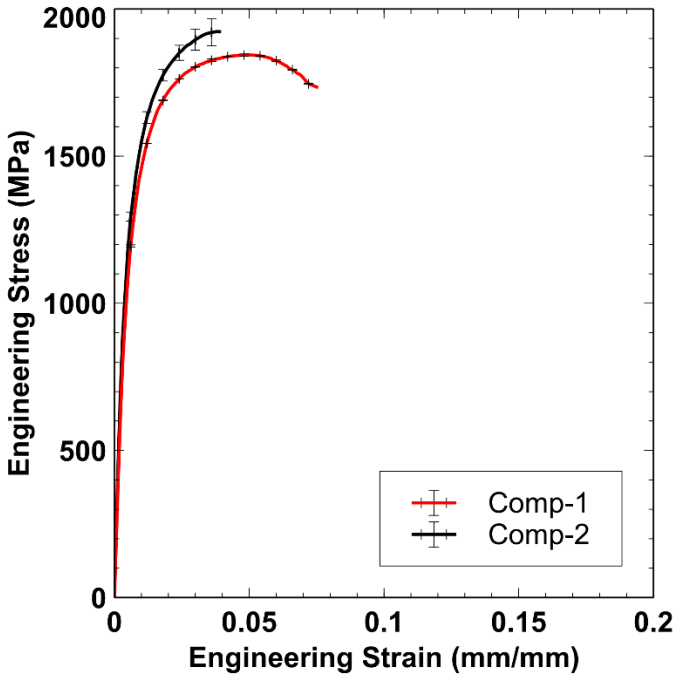

Figure 3.3 Stress-strain curves for Comp-2 and Comp-5 as received. Tension tests took place at 0.0254 mm/s constant crosshead speed [49].

Table 3.2 Mechanical properties of Comp-2 and Comp-5 from uniaxial tension at 0.0254 mm/s constant crosshead speed. YS is 0.2% offset yield strength, UTS is ultimate tensile strength, UE is uniform elongation, and TE is total elongation [49].

Sample	YS (MPa)	UTS (MPa)	UE (%)	TE (%)
Comp-2	1370	1844	5.00	7.60
Comp-5	1364	1923	3.80	4.00

The instantaneous n-exponent values in Figure 3.4 show similar strain hardening behavior for Comp-2 and Comp-5. Both have initially high n-exponent values that decrease sharply before steadily decreasing up to necking in the stress-strain curve. This behavior is similar to other TRIP steels with mostly ferrite microstructures. Both Comp-2 and Comp-5 were appropriate steels to

apply quenching and partitioning and determine if their ductility could be increased without losing too much strength.

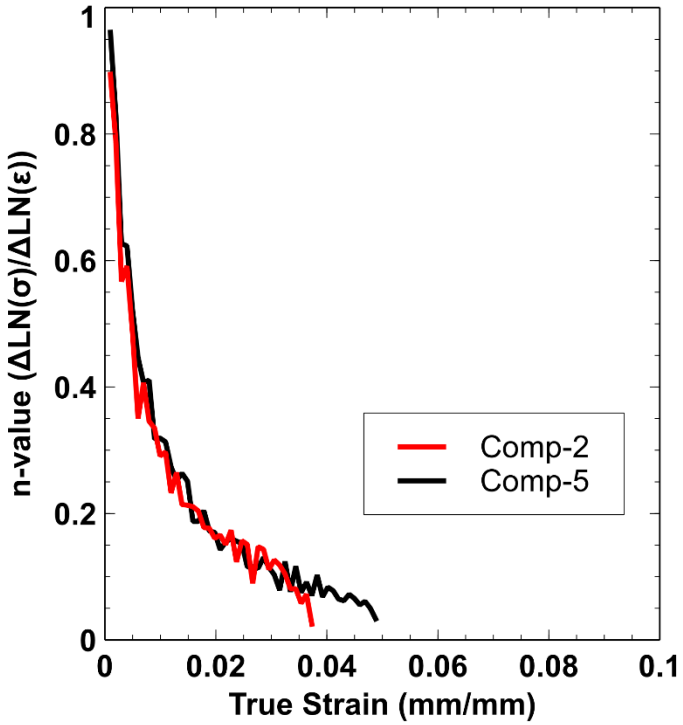

Figure 3.4 Instantaneous n-exponent values versus true strain for Comp-2 and Comp-5 as received [49].

3.3 Quenched and Partitioned TRIP Steel Mechanical Results

The mechanical results revealed enhanced ductility in the stress-strain curves of Comp-2 and Comp-5 (Figure 3.5) [49]. The mechanical properties (Table 3.3) for Comp-2 and Comp-5 show that the ultimate stress of Comp 2 was higher than Comp-5 (1354 MPa versus 1246 MPa). A possible reason is the quench temperature's (QT) location within martensite start and finish temperatures for Comp-2 and Comp-5. The 250ºC QT was closer to Comp-2's martensite finish temperature; thus, more martensite was present before partitioning, and Comp-2's strength was

higher [49]. Comp-5's martensite start temperature was closer to 250ºC QT; as a result, less martensite was present, causing the strength to lower. The total elongation for Comp-2 and Comp-5 were the same value (13.10%), suggesting Comp-5 had the greatest increase in ductility from as received material [49].

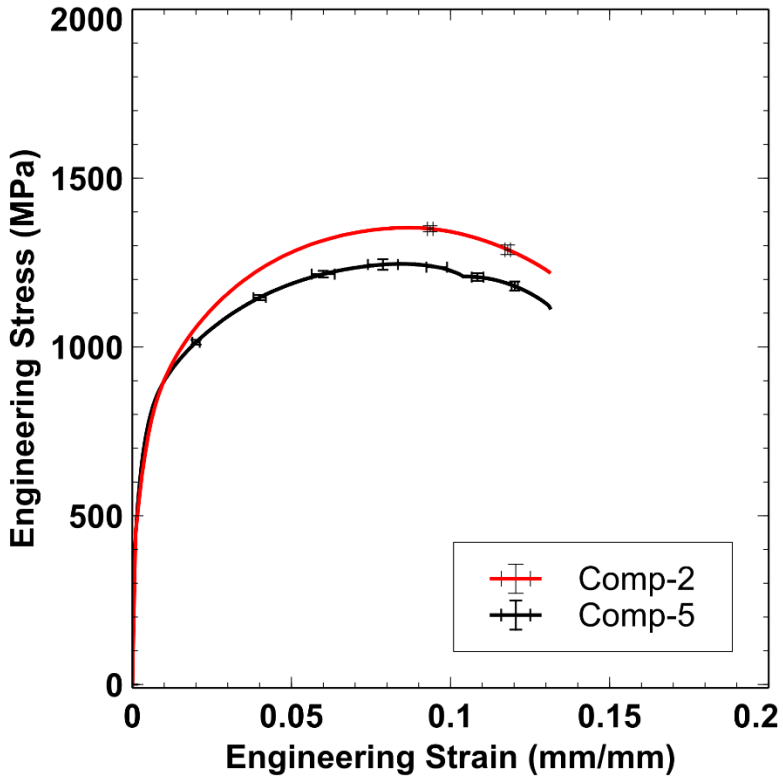

Figure 3.5 Engineering stress-strain behavior at 0.0254 mm/s constant crosshead speed of Comp-2 and Comp-5 quenched and partitioned. Comp-2 has higher strength, while both compositions exhibit similar ductility [49].

Table 3.3 Mechanical properties of Comp-2 and Comp-5. Yield Stress (YS) is 0.02% offset, US is ultimate strength, UE is uniform elongation, and TE is total elongation [49].

Sample	YS (MPa)	US (MPa)	UE (%)	TE (%)
Comp-2	877	1354	8.70	13.10
Comp-5	823	1246	8.40	13.10

Figure 3.6 shows the strain hardening behavior of Comp-2 and Comp-5 after quenching and partitioning [49]. Both curves are steady throughout deformation, suggesting TRIP effect occurred gradually. Hardness testing of Comp-2 and Comp-5 revealed a homogenous heat-treated zone within the gage length. Table 3.4 shows similar values for the middle and end of the gage length section. The Gleeble was able to produce a mostly uniform hot zone during the Q&P process [49].

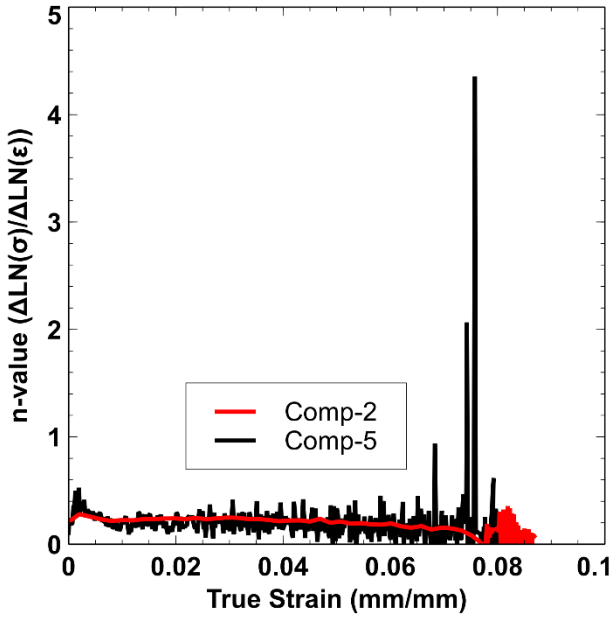

Figure 3.6 Instantaneous n-exponent values versus true strain for Comp-2 and Comp-5 after quenching and partitioning [49].

Table 3.4 Rockwell C-scale hardness values from four locations on dog bone samples of Comp-2 and Comp-5 after quenching and partitioning [49].

Sample	(1)	(2)	(3)	(4)
Comp-2 Quenched and Partitioned	42.6 ± 1.4	46.1 ± 0.6	41.3 ± 1.0	34.8 ± 0.2
Comp-5 Quenched and Partitioned	40.9 ± 0.4	40.1 ± 1.8	36.7 ± 0.4	33.1 ± 0.8

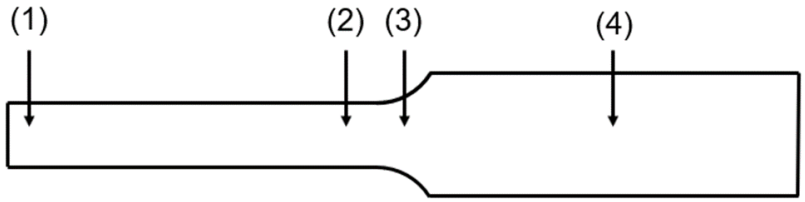

Figure 3.7 Location of hardness tests performed on ASTM E8 dog bone samples of Comp-2 and Comp-5 [49].

3.4 Hot-Rolled and Quenched TRIP Steel Microstructural Results

The starting microstructures for Comp-2 and Comp-5 were very different. Figure 3.8 shows the inverse pole figures overlaid with confidence index for Comp-2 and Comp-5 as received [49]. Comp-2's microstructure consists of elongated ferrite grains with some martensite islands, formed during the hot-rolling process. Comp-5's microstructure, however, shows equiaxed ferrite grains within a martensitic matrix, which suggests recrystallization occurred during hot-rolling. While the starting microstructures are different, the quenching and partitioning process applied involves full austenization; therefore, both steels had fully austenitic microstructures before quenching, only the austenite grain sizes were different due to the temperature difference in A_3 and austenitizing temperature (900ºC) [49].

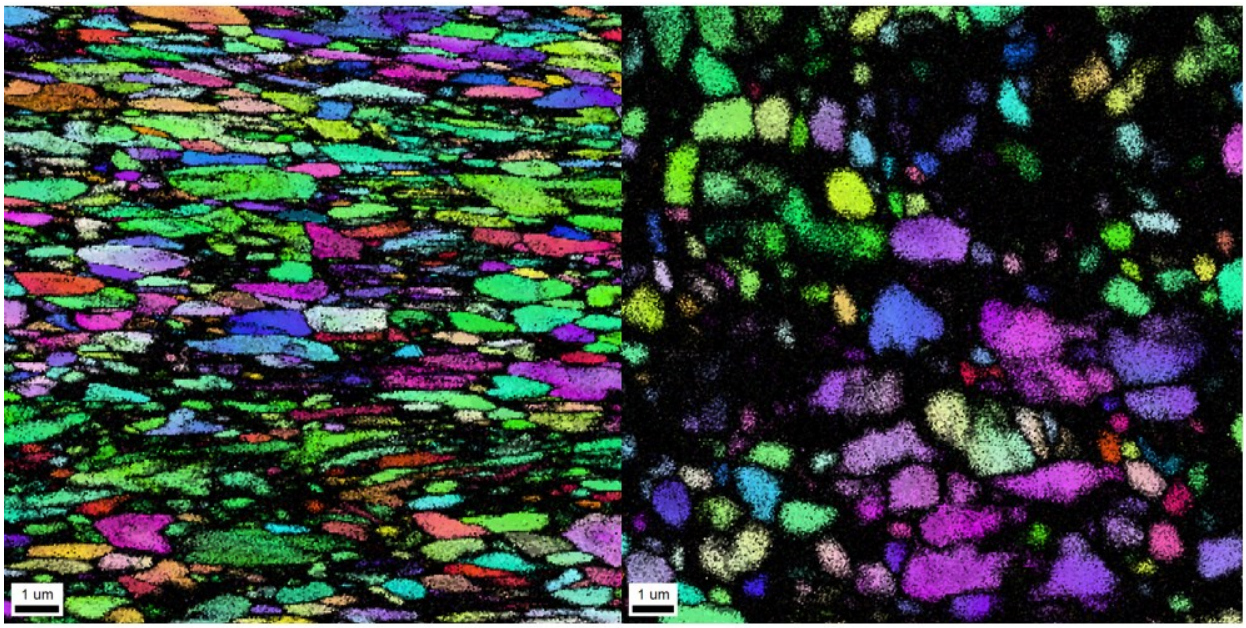

Figure 3.8 Inverse pole figures overlaid with confidence index for Comp-2 and Comp-5 in the hot-rolled and water quenched state. Comp-2 shows elongated ferrite grains with martensitic islands, while Comp-5 shows equiaxed ferrite grains within a martensitic matrix [49].

3.5 Quenched and Partitioned TRIP Steel Microstructural Results

Figure 3.9 and Figure 3.10 show (a) inverse pole figure, (b) phase composition, and (c) austenite orientation in the microstructure of Comp-2 and Comp-5, respectively [49]. Each figure is overlaid with confidence index. Martensite is colored red and retained austenite is colored in green. Comp-5 had a smaller amount of retained austenite (8.1%) compared to Comp-2 (10.4%). Austenite in both quenched and partitioned steels is located at the martensite grain boundaries. The chosen Q&P process was able to produce retained austenite and martensite in Comp-2 and Comp-5 which led to increase in ductility, as austenite mitigated strain incompatibility between martensite grains [49].

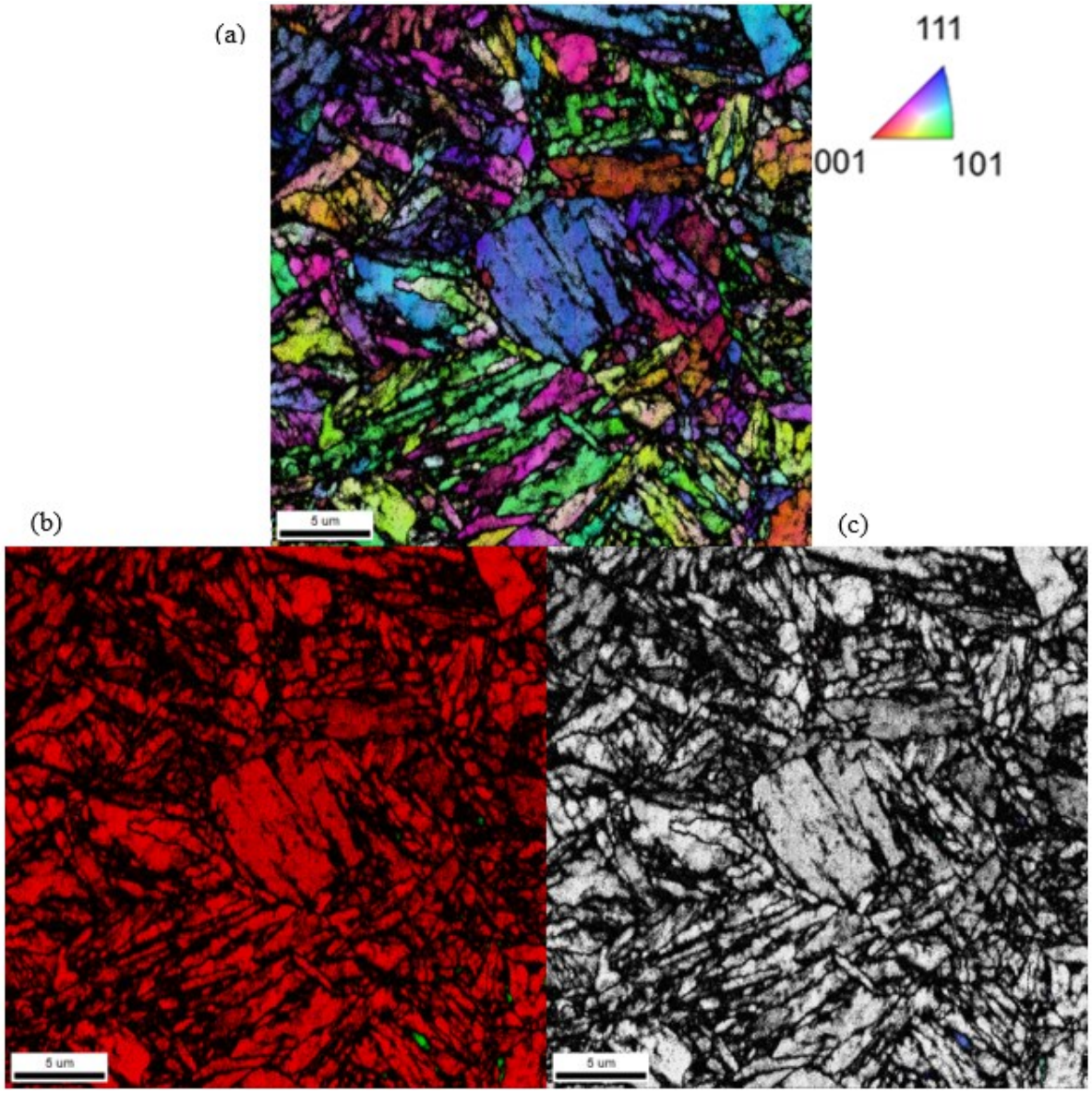

Figure 3.9 EBSD analyses of Comp-2 sample showing (a) an inverse pole figure, (b) phase map of martensite in red and austenite in green, and (c) an inverse pole figure of solely austenite. Each figure is overlaid with confidence index. Some austenite grains can be seen at the bottom right corner of the phase map and austenite inverse pole figure [49].

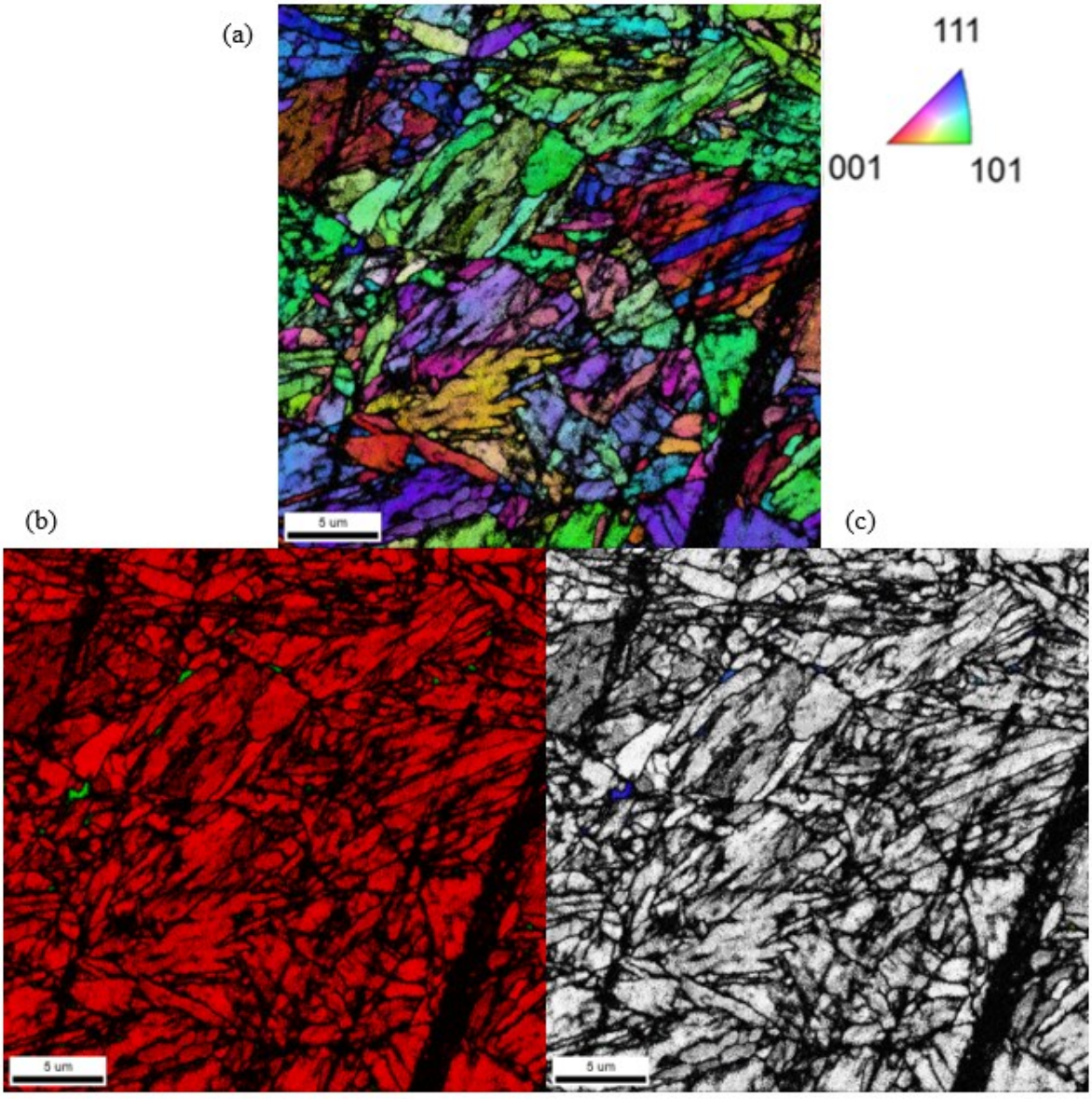

Figure 3.10 EBSD analyses of Comp-5 sample showing (a) an inverse pole figure, (b) phase map of martensite in red and austenite in green, and (c) an inverse pole figure of solely austenite revealing the exclusive location of austenite at the grain boundaries of martensite. Each figure is overlaid with confidence index [49].

3.6 Discussion about 3GAHSS Microstructure Design

We were able to increase the ductility of Comp-2 and Comp-5 through quenching and partitioning. Comp-2's total elongation increased by 79%, and Comp-5's total elongation increased by 228% [49]. Figure 3.11 shows the change in mechanical behavior before and after quenching and partitioning of Comp-2 and Comp-5. Both compositions benefited from an enhanced TRIP effect that delayed necking and increased ductility. Comp-2 and Comp-5 experienced a drop in Rockwell C-scale hardness values, indicative of increased volume fraction of retained austenite in their microstructures. Table 3.5 lists the before and after hardness values for Comp-2 and Comp-5. Comp-2 and Comp-5 experience a decrease in hardness of 19% and 20%, respectively [49].

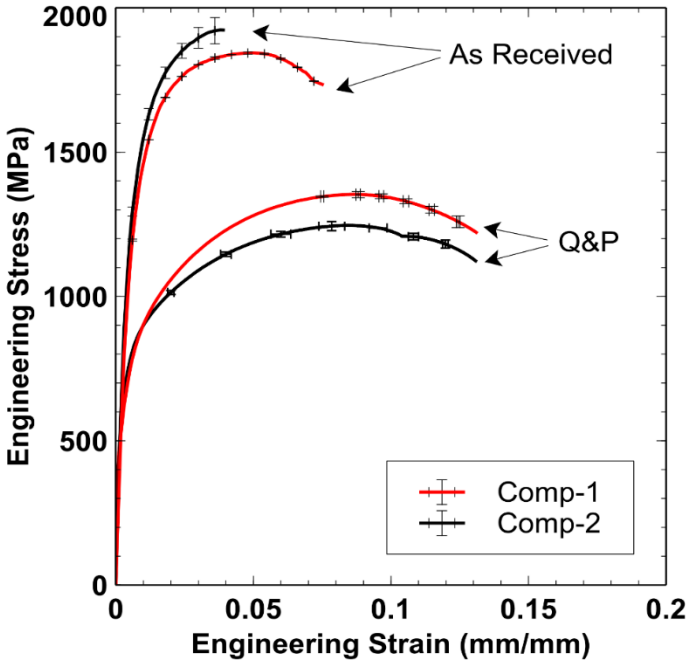

Figure 3.11 Stress-strain curve comparison of as received and Q&P Comp-2 and Comp-5 [49].

Table 3.5 Rockwell C-scale hardness values from four locations on dog bone samples of Comp-2 and Comp-5 after quenching and partitioning [49].

Sample	(1)	(2)	(3)	(4)	Average
Comp-2 As received	50.9 ± 0.2	50.6 ± 0.4	51.3 ± 0.6	51.2 ± 0.5	51.0 ± 0.5
Comp-5 As received	46.6 ± 1.6	47.5 ± 0.3	47.6 ± 0.3	48.1± 0.7	47.4 ± 1.0
Comp-2 Q&P	42.6 ± 1.4	46.1 ± 0.6	41.3 ± 1.0	34.8 ± 0.2	41.2 ± 4.4
Comp-5 Q&P	40.9 ± 0.4	40.1 ± 1.8	36.7 ± 0.4	33.1 ± 0.8	37.7 ± 3.4

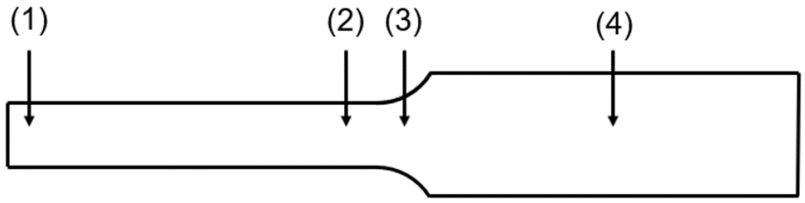

Figure 3.12 Schematic of hardness measurements taken from (1) middle gage length, (2) end of gage length, (3) transition to grip section, and (4) grip section [49].

Comparing the starting and final microstructures of Comp-2 and Comp-5, the phases change from ferrite to martensite/retained austenite [49]. Both compositions showed volume fractions of retained austenite stabilized at room temperature. Figure 3.13 shows the before and after microstructures of Comp-2 and Comp-5 with applied quenching and partitioning. Comp-5 had a higher volume fraction of austenite before partitioning than Comp-2 because of the 250ºC temperature. This temperature was closer to martensite start for Comp-5 than Comp-2; as such, the partitioning process parameters were not well optimized for this Comp-2, but Comp-2 had more retained austenite after partitioning, which led to superior mechanical properties [49].

Unfortunately, the Q&P process has been challenged by uncertainties of the resulting mechanical properties. Possible culprits of the high process variability are the high diffusivity and

reactivity of carbon. Small size, trapping sensitivity, and carbide affinity of carbon atoms have plagued the control of the process-microstructure property relationship. Despite the addition of silicon known to thermodynamically destabilize carbides [38], the uncertainties in mechanical properties are still high in Q&P steels. Comp-2 and Comp-5 seemed to have the right combination of C, Mn, and Nb contents to promote carbon clustering near grain boundaries; thus, they promoted austenite stabilization at the right place [49]. The additions of Nb seem counterintuitive because they have a strong affinity to carbon. However, Nb has a very slow diffusivity in iron and provides a suitable selection and control of high quenching rates and partitioning time and temperature [53]; thus, Nb can promote carbon atom clustering near grain boundaries of martensite [13]. Carbon clustering near grain boundaries and defects would strongly promote stability of austenite at those regions where high ductility is precisely needed; in fact, these regions are prone to hot spot and damage initiation and constitute a prime consideration for ductile microstructural design. Nb can also form small carbides during the high austenization temperature, which promotes grain boundary pinning and grain refinement. Small grains of pre-quenched austenite would lead to very small retained austenite phases which could be fully perfused by carbon atoms during partitioning. The large effect of composition on the required process parameters for promoting enough martensite-boundary austenite explains the great uncertainty affecting the Q&P approach toward 3GAHSS. Enough carbon and manganese should be added to segregate at the boundaries without the risk of forming carbides. The choice of the carbide former is also important to the microstructure optimization feasibility. The volume fraction of retained austenite has been heavily studied by several authors [6, 7, 9, 17-18], but the location of austenite has been less emphasized despite its importance to reduce strain incompatibilities between martensitic grains [56].

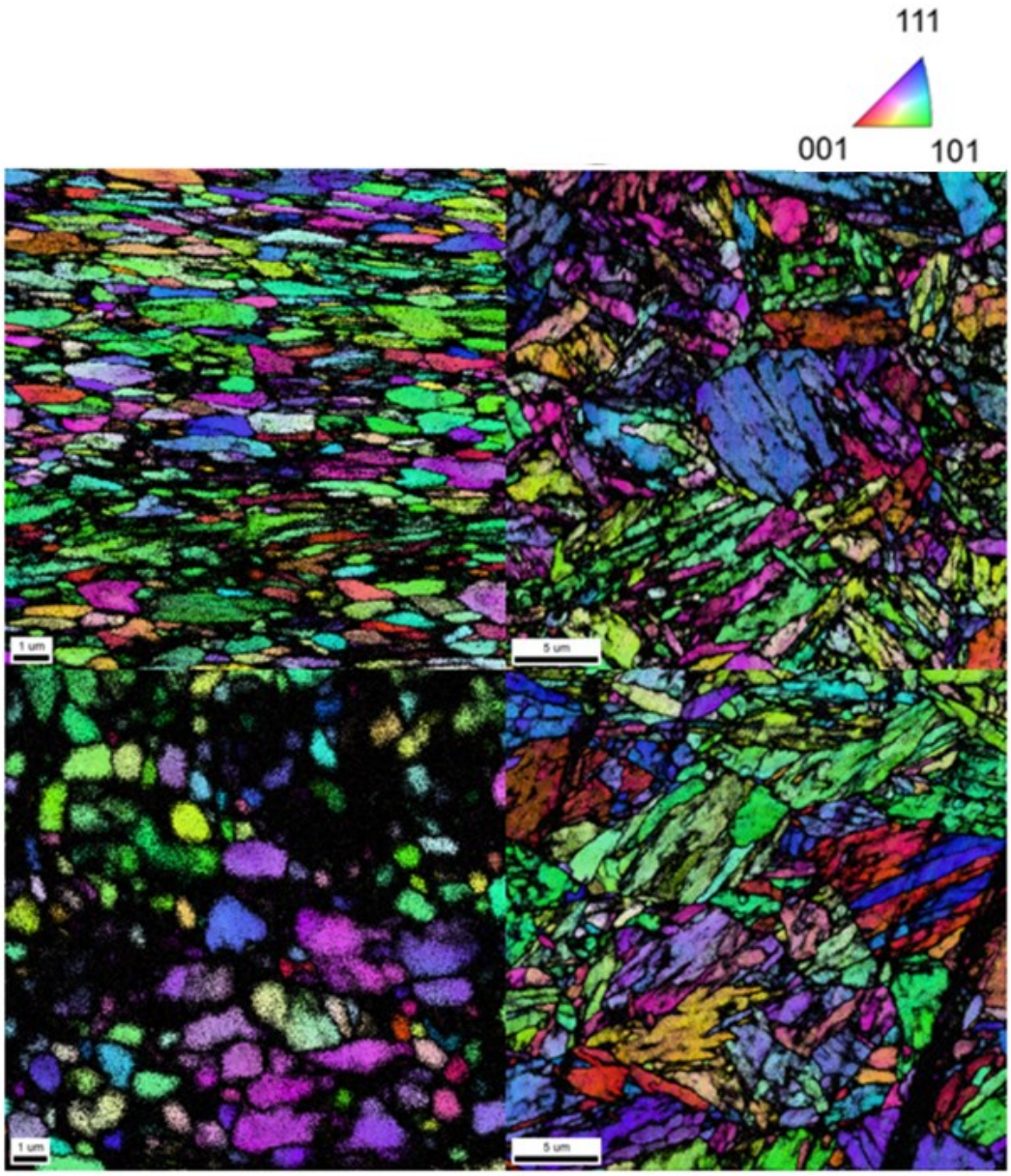

Figure 3.13 Inverse pole figures before and after quenching and partitioning of Comp-2 and Comp-5. Beginning microstructure is ferrite for both compositions which is transformed to martensite and retained austenite. Each figure is overlaid with confidence index [49].

The quenching and partitioning we applied to Comp-2 and Comp-5 was performed in a Gleeble thermo-mechanical simulator [49]. The vacuum level was 10^{-8} torr, and heating/cooling

rates had very precise control. Despite the highly controlled environment and heat-treatment profile, we could not increase the ductility of Comp-2 or Comp-5 to the values set by the Department of Energy (Figure 3.14). Previous attempts at these targets have not achieved these DOE values through quenching and partitioning [49]. The underlying reason for this discrepancy is the main component of the Q&P process – carbon. C has an affinity for many different microstructural features such as carbides and dislocations. Directing C to austenite during partitioning is a challenge, and even when successful, no amount of carbon can stabilize austenite sufficiently to achieve higher mechanical properties than previous research. We propose a limit of austenite stabilization through carbon during quenching and partitioning that prevents further enhancement of mechanical properties [49].

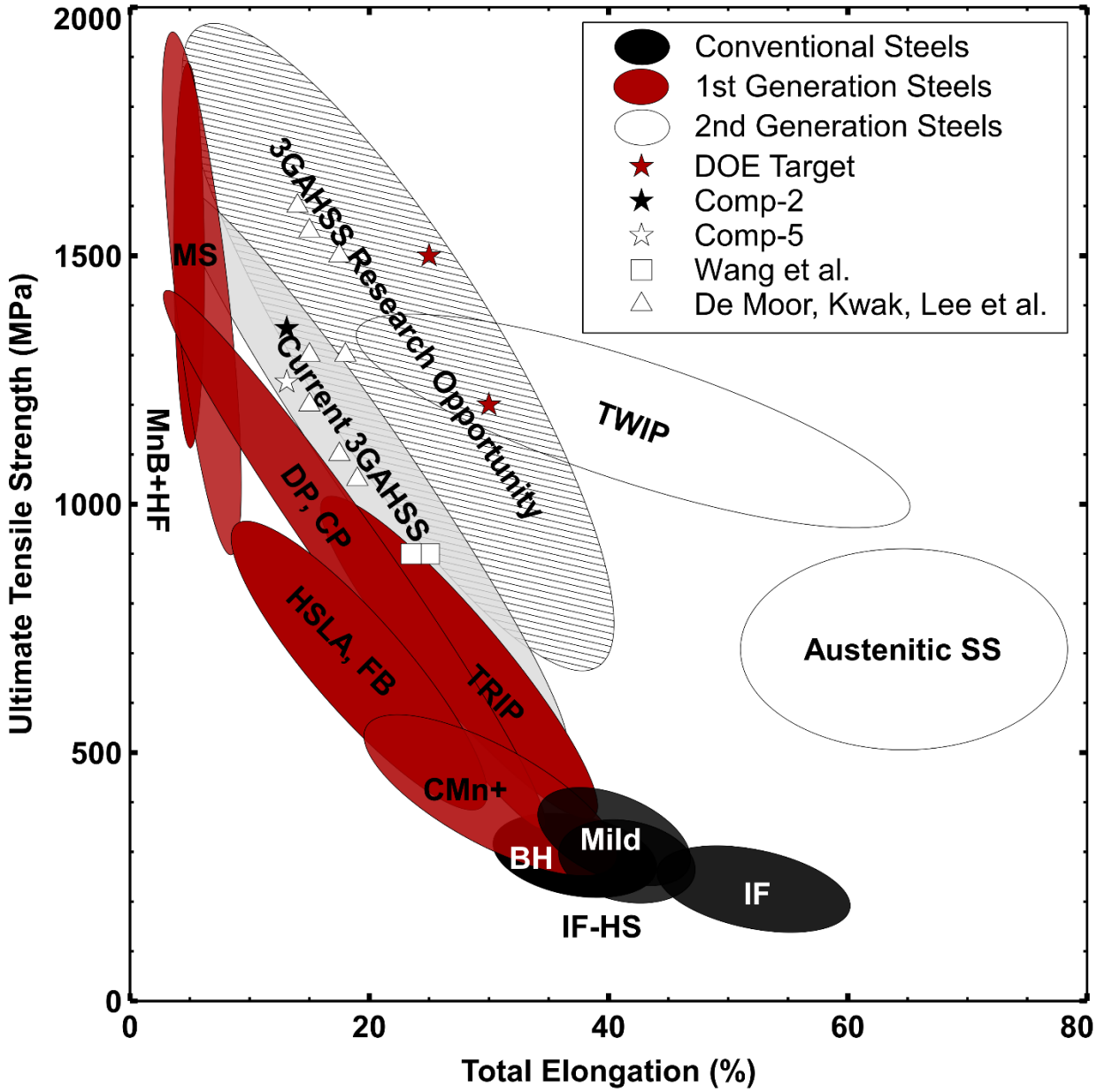

Figure 3.14 Steel generation chart showing Comp-2 (white star) and Comp-5 (black star) quenched and partitioned along with previous attempts at 3GAHSS by Wang et al., De Moor et al., Kwak et al., and Lee et al. [25, 49].

3.7 Conclusions about 3GAHSS Microstructure Design

In summary, gaining substantial ductility without losing much strength in cost-effective Fe-C-Mn-Si third generation advanced high strength steels by the quenching and partitioning process has not been demonstrated in this study. This combination is hard to achieve through Q&P due to impossible control of C. Stable austenite is crucial at the grain boundaries for securing high ductility; however, stabilization of austenite with C is not precise and shows a huge uncertainty in the mechanical properties. Figure 3.14 shows the mechanical properties of Comp-2 and Comp-5 after quenching and partitioning compared with previous steel generations. While both are located in the current third generation advanced high strength steel region, further improvement of mechanical properties is not possible through Q&P process. We hope to apply periodic intercritical annealing to medium manganese steels to secure mechanical properties beyond Comp-2 and Comp-5. Manganese is a more effective austenite stabilizer than C and can unlock 3GAHSS potential with a tailored heat-treatment.

REFERENCES

[1] J. Speer, D. K. Matlock, B. C. De Cooman, and J. G. Schroth, "Carbon partitioning into austenite after martensite transformation," *Acta Mater.*, vol. 51, no. 9, pp. 2611–2622, May 2003, doi: 10.1016/S1359-6454(03)00059-4.

[2] E. De Moor, S. Lacroix, A. J. Clarke, J. Penning, and J. G. Speer, "Effect of Retained Austenite Stabilized via Quench and Partitioning on the Strain Hardening of Martensitic Steels," *Metall. Mater. Trans. A*, vol. 39, no. 11, p. 2586, Jul. 2008, doi: 10.1007/s11661-008-9609-z.

[3] H. Y. Li, X. W. Lu, W. J. Li, and X. J. Jin, "Microstructure and Mechanical Properties of an Ultrahigh-Strength 40SiMnNiCr Steel during the One-Step Quenching and Partitioning Process," *Metall. Mater. Trans. A*, vol. 41, no. 5, pp. 1284–1300, May 2010, doi: 10.1007/s11661-010-0184-8.

[4] M. J. Santofimia, J. G. Speer, A. J. Clarke, L. Zhao, and J. Sietsma, "Influence of interface mobility on the evolution of austenite–martensite grain assemblies during annealing," *Acta Mater.*, vol. 57, no. 15, pp. 4548–4557, Sep. 2009, doi: 10.1016/j.actamat.2009.06.024.

[5] E. D. Moor, J. G. Speer, D. K. Matlock, J.-H. Kwak, and S.-B. Lee, "Effect of Carbon and Manganese on the Quenching and Partitioning Response of CMnSi Steels," *ISIJ Int.*, vol. 51, no. 1, pp. 137–144, 2011, doi: 10.2355/isijinternational.51.137.

[6] A. Soulami, K. S. Choi, Y. F. Shen, W. N. Liu, X. Sun, and M. A. Khaleel, "On deformation twinning in a 17.5% Mn–TWIP steel: A physically based phenomenological model," *Mater. Sci. Eng. A*, vol. 528, no. 3, pp. 1402–1408, Jan. 2011, doi: 10.1016/j.msea.2010.10.031.

[7] R. D. K. Misra, B. R. Kumar, M. Somani, and P. Karjalainen, "Deformation processes during tensile straining of ultrafine/nanograined structures formed by reversion in metastable austenitic steels," *Scr. Mater.*, vol. 59, no. 1, pp. 79–82, Jul. 2008, doi: 10.1016/j.scriptamat.2008.02.028.

[8] M. Hillert and J. Ågren, "On the definitions of paraequilibrium and orthoequilibrium," *Scr. Mater.*, vol. 50, no. 5, pp. 697–699.

[9] J. G. Speer, D. K. Matlock, B. C. DeCooman, and J. G. Schroth, "Comments on 'On the definitions of paraequilibrium and orthoequilibrium' by M. Hillert and J. Ågren, Scripta Materialia, 50, 697–9 (2004)," *Scr. Mater.*, vol. 52, no. 1, pp. 83–85, Jan. 2005, doi: 10.1016/j.scriptamat.2004.08.029.

[10] M. Hillert and J. Ågren, "Reply to comments on 'On the definition of paraequilibrium and orthoequilibrium,'" *Scr. Mater.*, vol. 52, no. 1, pp. 87–88, Jan. 2005, doi: 10.1016/j.scriptamat.2004.08.026.

[11] S. Keeler, M. Kimchi, and P. J. Mooney, "Advanced High-Strength Steels Application Guidelines Version 6.0," *WorldAutoSteel*, Apr. 2017.

[12] R. L. Miller, "Ultrafine-grained microstructures and mechanical properties of alloy steels," *Metall. Mater. Trans. B*, vol. 3, no. 4, pp. 905–912, Apr. 1972, doi: 10.1007/BF02647665.

[13] E. Navara, B. Bengtsson, and K. E. Easterling, "Austenite Formation in Manganese-Partitioning Dual-Phase Steel," *Mater. Sci. Technol.*, vol. 2, pp. 1196–1201, 1986.

[14] G. R. Speich, V. A. Demarest, and R. L. Miller, "Formation of Austenite During Intercritical Annealing of Dual-Phase Steels," *Metall. Mater. Trans. A*, vol. 12, no. 8, pp. 1419–1428, Aug. 1981, doi: 10.1007/BF02643686.

[15] S. Sun and M. Pugh, "Manganese partitioning in dual-phase steel during annealing," *Mater. Sci. Eng. A*, vol. 276, no. 1, pp. 167–174, Jan. 2000, doi: 10.1016/S0921-5093(99)00261-0.

[16] J. Lis, A. Lis, and C. Kolan, "Manganese partitioning in low carbon manganese steel during annealing," *Mater. Charact.*, vol. 59, no. 8, pp. 1021–1028, Aug. 2008, doi: 10.1016/j.matchar.2007.08.020.

[17] E. De Moor, D. K. Matlock, J. G. Speer, and M. J. Merwin, "Austenite stabilization through manganese enrichment," *Scr. Mater.*, vol. 64, no. 2, pp. 185–188, Jan. 2011, doi: 10.1016/j.scriptamat.2010.09.040.

[18] D. P. Koistinen and R. E. Marburger, "A general equation prescribing the extent of the austenite-martensite transformation in pure iron-carbon alloys and plain carbon steel," *Acta Mater.*, vol. 59–60, 1959.

[19] S. Lee, S.-J. Lee, S. Santhosh Kumar, K. Lee, and B. C. D. Cooman, "Localized Deformation in Multiphase, Ultra-Fine-Grained 6 Pct Mn Transformation-Induced Plasticity Steel," *Metall. Mater. Trans. A*, vol. 42, no. 12, pp. 3638–3651, Dec. 2011, doi: 10.1007/s11661-011-0636-9.

[20] P. J. Gibbs, E. De Moor, M. J. Merwin, B. Clausen, J. G. Speer, and D. K. Matlock, "Austenite Stability Effects on Tensile Behavior of Manganese-Enriched-Austenite Transformation-Induced Plasticity Steel," *Metall. Mater. Trans. A*, vol. 42, no. 12, pp. 3691–3702, Dec. 2011, doi: 10.1007/s11661-011-0687-y.

[21] B. C. De Cooman, P. Gibbs, S. Lee, and D. K. Matlock, "Transmission Electron Microscopy Analysis of Yielding in Ultrafine-Grained Medium Mn Transformation-Induced Plasticity Steel," *Metall. Mater. Trans. A*, vol. 44, no. 6, pp. 2563–2572, Jun. 2013, doi: 10.1007/s11661-013-1638-6.

[22] P. J. Gibbs *et al.*, "Strain partitioning in ultra-fine grained medium-manganese transformation induced plasticity steel," *Mater. Sci. Eng. A*, vol. 609, pp. 323–333, Jul. 2014, doi: 10.1016/j.msea.2014.03.120.

[23] Z. H. Cai, H. Ding, R. D. K. Misra, and Z. Y. Ying, "Austenite stability and deformation behavior in a cold-rolled transformation-induced plasticity steel with medium manganese content," *Acta Mater.*, vol. 84, pp. 229–236, Feb. 2015, doi: 10.1016/j.actamat.2014.10.052.

[24] E. D. Moor, S. Lacroix, A. J. Clarke, J. Penning, and J. G. Speer, "Effect of Retained Austenite Stabilized via Quench and Partitioning on the Strain Hardening of Martensitic Steels," *Metall. Mater. Trans. A*, vol. 39, no. 11, p. 2586, Jul. 2008, doi: 10.1007/s11661-008-9609-z.

[25] J. G. Speer, E. D. Moor, K. O. Findley, D. K. Matlock, B. C. D. Cooman, and D. V. Edmonds, "Analysis of Microstructure Evolution in Quenching and Partitioning Automotive Sheet Steel," *Metall. Mater. Trans. A*, vol. 42, no. 12, p. 3591, Sep. 2011, doi: 10.1007/s11661-011-0869-7.

[26] G. A. Thomas, J. G. Speer, and D. K. Matlock, "Quenched and Partitioned Microstructures Produced via Gleeble Simulations of Hot-Strip Mill Cooling Practices," *Metall. Mater. Trans. A*, vol. 42, no. 12, pp. 3652–3659, Dec. 2011, doi: 10.1007/s11661-011-0648-5.

[27] G. Gao, H. Zhang, X. Gui, P. Luo, Z. Tan, and B. Bai, "Enhanced ductility and toughness in an ultrahigh-strength Mn–Si–Cr–C steel: The great potential of ultrafine filmy retained austenite," *Acta Mater.*, vol. 76, pp. 425–433, Sep. 2014, doi: 10.1016/j.actamat.2014.05.055.

[28] J. G. Speer, A. M. Streicher, D. K. Matlock, F. C. Rizzo, and G. Krauss, "Quenching and partitioning: a fundamentally new process to create high strength TRIP sheet microstructures," *Austenite Deform. Decompos.*, pp. 502–522, 2003.

[29] A. Clarke, J. G. Speer, D. K. Matlock, F. C. Rizzo, D. V. Edmonds, and K. He, "Microstructure and Carbon Partitioning in a 0.19%C- 1.59%Mn-1.63%Si TRIP Sheet Steel Subjected to Quenching and Partitioning (Q&P)," *Solid-Solid Phase Transform. Inorg. Mater.*, vol. 2, pp. 100–108, 2005.

[30] M. J. Santofimia, L. Zhao, and J. Sietsma, "Microstructural Evolution of a Low-Carbon Steel during Application of Quenching and Partitioning Heat Treatments after Partial Austenitization," *Metall. Mater. Trans. A*, vol. 40, no. 1, p. 46, Jan. 2009, doi: 10.1007/s11661-008-9701-4.

[31] N. Zhong, X. D. Wang, L. Wang, and Y. H. Rong, "Enhancement of the mechanical properties of a Nb-microalloyed advanced high-strength steel treated by quenching–partitioning–tempering process," *Mater. Sci. Eng. A*, vol. 506, no. 1, pp. 111–116, Apr. 2009, doi: 10.1016/j.msea.2008.11.014.

[32] A. J. Clarke, J. G. Speer, D. K. Matlock, F. C. Rizzo, D. V. Edmonds, and M. J. Santofimia, "Influence of carbon partitioning kinetics on final austenite fraction during quenching and partitioning," *Scr. Mater.*, vol. 61, no. 2, pp. 149–152, Jul. 2009, doi: 10.1016/j.scriptamat.2009.03.021.

[33] S. J. Kim, "Effects of Manganese Content and Heat Treatment Condition on Mechanical Properties and Microstructures of Fine-Grained Low Carbon TRIP-Aided Steels," *Mater. Sci. Forum*, vol. 638–642, pp. 3313–3318, Jan. 2010, doi: 10.4028/www.scientific.net/MSF.638-642.3313.

[34] D. H. Kim, J. G. Speer, H. S. Kim, and B. C. D. Cooman, "Observation of an Isothermal Transformation during Quenching and Partitioning Processing," *Metall. Mater. Trans. A*, vol. 40, no. 9, pp. 2048–2060, Sep. 2009, doi: 10.1007/s11661-009-9891-4.

[35] G. P. Krielaart and S. van der Zwaag, "Kinetics of $\gamma \rightarrow \alpha$ phase transformation in Fe-Mn alloys containing low manganese," *Mater. Sci. Technol.*, vol. 14, no. 1, pp. 10–18, Jan. 1998, doi: 10.1179/mst.1998.14.1.10.

[36] M. J. Santofimia, L. Zhao, R. Petrov, C. Kwakernaak, W. G. Sloof, and J. Sietsma, "Microstructural development during the quenching and partitioning process in a newly designed low-carbon steel," *Acta Mater.*, vol. 59, no. 15, pp. 6059–6068, Sep. 2011, doi: 10.1016/j.actamat.2011.06.014.

[37] H. Huang, O. Matsumura, and T. Furukawa, "Retained Austenite in Low Carbon, Manganese Steel after Intercritical Heat Treatment," *Mater. Sci. Technol.*, vol. 10, pp. 621–626, 1994.

[38] M. J. Merwin, "Low-Carbon Manganese TRIP Steels," *Materials Science Forum*, 2007. https://www.scientific.net/msf.539-543.4327 (accessed Sep. 15, 2019).

[39] H. M. Rietveld, "A profile refinement method for nuclear and magnetic structures," *J. Appl. Crystallogr.*, vol. 2, pp. 65–71, 1969.

[40] Q. Han, Y. Zhang, and L. Wang, "Effect of Annealing Time on Microstructural Evolution and Deformation Characteristics in 10Mn1.5Al TRIP Steel," *Metall. Mater. Trans. A*, vol. 46, no. 5, pp. 1917–1926, May 2015, doi: 10.1007/s11661-015-2822-7.

[41] B. C. De Cooman, S. J. Lee, S. Shin, E. J. Seo, and J. G. Speer, "Combined Intercritical Annealing and Q&P Processing of Medium Mn Steel," *Metall. Mater. Trans. A*, vol. 48, no. 1, pp. 39–45, Jan. 2017, doi: 10.1007/s11661-016-3821-z.

[42] R. Rana, P. J. Gibbs, E. De Moor, J. G. Speer, and D. K. Matlock, "A Composite Modeling Analysis of the Deformation Behavior of Medium Manganese Steels," *Steel Res. Int.*, vol. 86, no. 10, pp. 1139–1150, Oct. 2015, doi: 10.1002/srin.201400577.

[43] A. K. Chandan, G. K. Bansal, J. Kundu, J. Chakraborty, and S. G. Chowdhury, "Effect of prior austenite grain size on the evolution of microstructure and mechanical properties of an intercritically annealed medium manganese steel," *Mater. Sci. Eng. A*, vol. 768, p. 138458, Dec. 2019, doi: 10.1016/j.msea.2019.138458.

[44] S. Okamoto, D. K. Matlock, and G. Krauss, "The transition from serrated to non-serrated flow in low-carbon martensite at 150°C," *Scr. Metall. Mater.*, vol. 25, no. 1, pp. 39–44, Jan. 1991, doi: 10.1016/0956-716X(91)90350-A.

[45] E. Paravicini Bagliani, M. J. Santofimia, L. Zhao, J. Sietsma, and E. Anelli, "Microstructure, tensile and toughness properties after quenching and partitioning treatments of a medium-carbon steel," *Mater. Sci. Eng. A*, vol. 559, pp. 486–495, Jan. 2013, doi: 10.1016/j.msea.2012.08.130.

[46] G. A. Thomas, E. De Moor, and J. G. Speer, "Tensile Properties Obtained by Q&P Processing of Mn-Ni Steels With Room Temperature Quench Temperatures," *Intl Symp New Dev. Adv. High-Strength Sheet Steels*, 2013.

[47] R. Rana, D. K. Matlock, J. G. Speer, and E. De Moor, "Effects of Strain Rate and Temperature on the Mechanical Properties of Medium Manganese Steels," United States Automotive Materials Partnership LLC (USAMP LLC), DOE-USAMP-05976-8, Nov. 2016. Accessed: Jun. 08, 2020. [Online]. Available: https://www.osti.gov/biblio/1363777.

[48] A. Dutta, D. Ponge, S. Sandlöbes, and D. Raabe, "Strain partitioning and strain localization in medium manganese steels measured by in situ microscopic digital image correlation," *Materialia*, vol. 5, p. 100252, Mar. 2019, doi: 10.1016/j.mtla.2019.100252.

[49] M. Cagle *et al.*, "Carbon Limitation of Stabilizing Austenite Through Quenching and Partitioning Approach for Third Generation Advanced High Strength Steels (unpublished)," Aug. 2020.

[50] M. Cagle *et al.*, "Austenite Stability Investigation of Room Temperature Quenched and Partitioned Steel (unpublished)," Aug. 2020.

[51] M. Cagle *et al.*, "Enhanced Ductility Through Periodic Intercritical Annealing of Medium Manganese Steel (unpublished)," Aug. 2020.

[52] P. Bicao, W. Jianhua, S. Xuping, L. Zhi, and Y. Fucheng, "Effects of zinc bath temperature on the coatings of hot-dip galvanizing," *Surf. Coat. Technol.*, vol. 202, no. 9, pp. 1785–1788, Feb. 2008, doi: 10.1016/j.surfcoat.2007.07.044.

[53] M. Charleux, W. J. Poole, M. Militzer, and A. Deschamps, "Precipitation behavior and its effect on strengthening of an HSLA-Nb/Ti steel," *Metall. Mater. Trans. A*, vol. 32, no. 7, pp. 1635–1647, Jul. 2001, doi: 10.1007/s11661-001-0142-6.

[54] J. Kähkönen *et al.*, "Quenched and Partitioned CMnSi Steels Containing 0.3 wt.% and 0.4 wt.% Carbon," *JOM*, vol. 68, no. 1, pp. 210–214, Jan. 2016, doi: 10.1007/s11837-015-1620-4.

[55] K. Zhang, M. Zhang, Z. Guo, N. Chen, and Y. Rong, "A new effect of retained austenite on ductility enhancement in high-strength quenching–partitioning–tempering martensitic steel," *Mater. Sci. Eng. A*, vol. 528, no. 29, pp. 8486–8491, Nov. 2011, doi: 10.1016/j.msea.2011.07.049.

[56] H. S. Zhao *et al.*, "Analysis of the relationship between retained austenite locations and the deformation behavior of quenching and partitioning treated steels," *Mater. Sci. Eng. A*, vol. 649, pp. 18–26, Jan. 2016, doi: 10.1016/j.msea.2015.09.088.